Phase shift invariant imaging of coherent sources (PSIICOS) from MEG data

A. Ossadtchi [a,b,*], D. Altukhov [b,c], K. Jerbi [d,e]

[a] Institute for Cognitive Neuroscience, National Research University Higher School of Economics, Moscow, Russian Federation
[b] Computer Science Faculty, National Research University Higher School of Economics, Moscow, Russian Federation
[c] Moscow State University of Pedagogics and Education, MEG-centre, Moscow, Russian Federation
[d] CoCo Lab, Psychology Department, University of Montreal, Montreal, QC, Canada
[e] MEG Unit, University of Montreal, Montreal, QC, Canada

A B S T R A C T

Increasing evidence suggests that neuronal communication is a defining property of functionally specialized brain networks and that it is implemented through synchronization between population activities of distinct brain areas. The detection of long-range coupling in electroencephalography (EEG) and magnetoencephalography (MEG) data using conventional metrics (such as coherence or phase-locking value) is by definition contaminated by spatial leakage. Methods such as imaginary coherence, phase-lag index or orthogonalized amplitude correlations tackle spatial leakage by ignoring zero-phase interactions. Although useful, these metrics will by construction lead to false negatives in cases where true zero-phase coupling exists in the data and will underestimate interactions with phase lags in the vicinity of zero. Yet, empirically observed neuronal synchrony in invasive recordings indicates that it is not uncommon to find zero or close-to-zero phase lag between the activity profiles of coupled neuronal assemblies.

Here, we introduce a novel method that allows us to mitigate the undesired spatial leakage effects and detect zero and near zero phase interactions. To this end, we propose a projection operation that operates on sensor-space cross-spectrum and suppresses the spatial leakage contribution but retains the true zero-phase interaction component. We then solve the network estimation task as a source estimation problem defined in the product space of interacting source topographies. We show how this framework provides reliable interaction detection for all phase-lag values and we thus refer to the method as Phase Shift Invariant Imaging of Coherent Sources (PSIICOS).

Realistic simulations demonstrate that PSIICOS has better detector characteristics than existing interaction metrics. Finally, we illustrate the performance of PSIICOS by applying it to real MEG dataset recorded during a standard mental rotation task. Taken together, using analytical derivations, data simulations and real brain data, this study presents a novel source-space MEG/EEG connectivity method that overcomes previous limitations and for the first time allows for the estimation of true zero-phase coupling via non-invasive electrophysiological recordings.

1. Introduction

The rapidly growing field of brain connectomics provides compelling evidence for a prominent role of functional and structural connectivity in mediating healthy brain function. It is now widely accepted that behavior is determined to a great extent by the coordinated activity of interacting cortical areas (e.g. Varela et al. (2001), Baker et al. (2014), Ossadtchi et al. (2010), Bastin et al. (2017), Luo et al. (2012), Jerbi et al. (2007)). Established research points to a prominent role of brain networks (van den Heuvel et al. (2012)) and neuronal rhythms (Buzsaki, 2006, Schnitzler and Gross (2005), Foster et al. (2016)) in providing mechanistic processes and dynamic brain-wide architectures. Collectively, such networks of oscillatory brain patterns provide a rich repertoire of neuronal communication paths necessary for cognition (Fries (2015)).

Beyond the spatial structure of a network, which is given by its nodes and edges, the time-varying and frequency-dependent strength of the interactions are critical. They are thought to capture the dynamic nature of such aggregations that coalesce and de-coalesce over time reflecting the complex structure of information flow in the brain. Therefore, the identification and characterization of the spatial, temporal and spectral

---

patterns of such interactions through electrophysiology is necessary in order to foster novel insights into the basic mechanisms and functional role of brain connectivity (Varela et al. (2001)). Despite important contributions from neuroimaging modalities, such as functional magnetic resonance imaging (fMRI), the detailed fine-grained dynamics are only amenable to electrophysiological measurement techniques such as electroencephalography (EEG), intracranial EEG and magnetoencephalography (MEG). When combined with source estimation techniques, MEG offers a unique combination of sub-centimeter spatial accuracy with millisecond-range temporal resolution (Hamalainen et al. (1993), Baillet et al. (2001), Gross et al. (2013)).

Considerable effort has been directed towards developing metrics and methodological frameworks to increase the diversity and reliability of cortical interaction measures. The large number of methods implemented and used over the last decades cover a wide range of approaches ranging from standard time and frequency-domain interaction metrics (such as correlation and coherence) to measures that quantify specific dimensions of signal coupling, such as phase-based or band-limited amplitude relationships, directionality, cross-frequency interactions or non-linear associations (Bastos and Schoffelen (2016), Marzetti et al. (2008), Schoffelen and Gross (2009), Colclough et al. (2016), Colclough et al. (2015), Greenblatt et al. (2012), Kaminski and Blinowska (2014), Hillebrand and Stam (2014), Nolte et al. (2004b), Lachaux et al. (1999), O'Neill et al., Brookes et al. (2012), Brookes et al. (2011), Hillebrand et al. (2012), Hipp et al. (2012), Vinck et al. (2011), Stam et al. (2007), Chella et al. (2016), Chella et al. (2015), Soto et al. (2016), Wibral et al. (2011), Ioannides et al. (2000), Baccalá and Sameshima (2001)).

One of the most prominent challenges that faces non-invasive MEG/EEG connectivity estimation is the spatial leakage effect which significantly complicates non-invasive studies of connectivity. Nolte et al. (2004a) suggested the use of the imaginary part of coherency as a solution to the spatial leakage issue; by ignoring the real component, imaginary coherence is *de facto* insensitive to zero-phase interactions. Since signal leakage is instantaneous, this method guarantees that any detected coupling reflects true physiological interaction. This was followed by further innovative measures based solely on the imaginary part of the cross-spectrum such as the Phase Lag Index (PLI) (Stam et al. (2007)) and its weighted version (wPLI) (Vinck et al. (2011)). These and other related metrics such as orthogonalized envelope correlation (Hipp et al. (2012), Colclough et al. (2015)) have now been widely adopted. Yet, despite providing an important pragmatic step forward, these metrics can underestimate true coupling because they are by construction blind to true physiological zero-phase interactions if any are present among the signals.

Another often overlooked limitation arises from the fact that the imaginary part of the source space coherence varies as a function of the sine of the phase lag between the coupled time series. Therefore, the imaginary part has sensitivity that is maximal at 90° phase difference and gradually drops to zero as the phase delay approaches zero. As a result, in cases where the coupled sources have near-zero time lags, the measures of coupling that exploit the imaginary part of cross-spectrum represent a low SNR signal.

In other words, not only are these metrics blind to zero-phase lag interactions, but their sensitivity is weak for phase lags approaching zero. Ironically, in many cases, empirically observed neuronal synchrony is characterized by a vanishing or very small phase lag between the time series of coupled neuronal ensembles (e.g. Roelfsema et al. (1997); Singer (1999); Engel et al., 2001). Indeed, true physiological zero-lag and near-zero lag coupling patterns may have several explanations. Macro-scale analysis shows that two cortical areas engaged in bidirectional interaction are likely to generate near-zero phase-lag synchrony as a result of reciprocal interaction or positively correlated common input (Rajagovindan and Ding (2008)). Moreover, near-zero lag coupling scenario may also be linked to the effect of detuning of synchronized populations with slightly different dynamical properties in order to adapt to a global rhythm (Pikovsky et al. (2001), Schuster and Wagner (1989)).

Therefore, in order to map cortical networks in healthy subjects under a wide range of experimental conditions and exercise freedom in fine-tuning the experimental designs it is important to develop synchrony detection techniques which are unaffected by signal leakage (MEG field spread, or EEG volume conduction) and that also work for zero- and near-zero phase lagged coupling. To the best of our knowledge, none of the interaction measures currently available allow for an assessment of linear zero-phase coupling that cannot be attributed to spatial leakage (i.e. true instantaneous coupling). Achieving this is precisely the aim of the present study, where we derive a new framework for the non-invasive estimation of connectivity with lag-invariant sensitivity.

Most MEG and EEG data synchrony analysis methods start with estimating cortical source activation time series, which are subsequently used for source-space analysis of coupling. This approach leads to propagation of time series estimation errors to the synchrony metrics used and causes variable performances depending on the inverse method chosen (Hincapie et al., 2016, 2017). While this approach (i.e. source-estimation followed by interaction measurement) might be inevitable when probing non-linear interaction effects, linear interactions can be studied using promising and intuitive approaches based on utilization of the generative model of sensor space cross-spectrum. As a matter of fact, an approach exploiting the spatial structure of the imaginary part of the observed cross-spectrum via subspace correlation metrics has been developed some time ago by Ewald et al. (2014). However, as discussed above, the use of the imaginary part of the cross-spectrum entails weaker sensitivity for near-zero lag coupling, compared to larger phase lags.

In the new method proposed here, we start with a generative model of the observed cross-spectrum of sensor signals and utilize the fact that the sensor space cross-spectrum is a linear combination of the outer products of interacting source topographies. The coefficients of such linear combinations are source-space cross-spectrum values. We then consider the vectorized form of this model and demonstrate that a simple projection operation defined in the product space of sensor signals can be used to alleviate the effects of spatial leakage (SL) on the real part of the cross-spectrum. Next, we examine the properties of the suggested procedure by means of Monte-Carlo simulations and show that such debiasing of the real part of the cross-spectrum delivers detectability of zero phase lag coupling as well as better sensitivity to near-zero lag coupling compared to the methods exploiting only the imaginary part of the cross-spectrum.

Moreover, in the last section of this paper, we illustrate the use of the proposed technique by applying it to a freely available real MEG dataset recorded during the mental rotation of wrist images. Using the proposed method, we identified physiologically plausible interhemispheric beta-band networks connecting the ventral visual pathway with hand-related sensorimotor areas and also observed gamma band coupling between hand-related sensory-motor sites, temporal pole and the orbitofrontal cortex. A more standard approach based on the use of the imaginary part of coherence only identified the beta-band interhemispheric coupling between the hand representation areas of the sensorimotor cortex, but not the above-mentioned gamma band interactions.

To the best of our knowledge, the proposed method is the first that can measure instantaneous leakage-free coupling represented in the real part of the sensor-space cross-spectrum. In addition, it also overcomes the reduced sensitivity of previous metrics to near-zero phase-lag coupling.

2. Methods

2.1. MEEG signal model and preliminaries

According to a most general formulation, MEEG data recorded by a $K-$ sensor array can be written as the following linear combination

$$\mathbf{x}^{tot}(t) = \mathbf{Ae}(t) + \mathbf{Gs}(t) + \mathbf{Bz}(t) + \mathbf{n}(t) \tag{1}$$

This model is exhaustive and explicitly includes the following four

components:

- $\mathbf{Ae}(t)$ — the contribution of the stimulus-locked activity to the measured signal $\mathbf{x}(t)$. This activity gives rise to the conventional evoked response fields that can be estimated from the data by the stimulus-locked averaging operation. This component is represented by the matrix of topographies $\mathbf{A} = [\mathbf{a}_1, ..., \mathbf{a}_N]$ of sources whose time series $\mathbf{e}(t) = [e_1(t), ..., e_N(t)]^T$ are phase-locked to the task onset moments marked by the stimulus signal. Note, that this component may be responsible for the trivial result of the phase-coupling analysis. The two sources whose activity is locked to the stimulus will automatically appear coupled to each other. Such coupling is not necessarily instantaneous and depends on the mutual morphology of the two evoked responses.
- $\mathbf{Gs}(t)$ — coherent brain activity that is not *phase-locked* to an experimental event. This component consists of two parts. The first one corresponds to the induced brain responses that occur in accordance with the stimulus, albeit, with random phase w.r.t. the task onset. It is their envelope that is locked to the stimulus. While the phase of individual source activations is *not* locked to the stimulus, the sources from this component group into clicks with activation phase *difference* aligned to the stimulus. These very groups of coupled sources are the targets of our analysis. The second part contributing to this component comes from the background activity produced by a finite set of brain sources whose coherence is either transient or persistent but unrelated to the task events. It is important to note that in the cross-spectrum computed using stimulus-locked averaging, contributions from sources coming from the first part (event-related) will typically dominate over those from the second part (spontaneous). Formally, we can represent both parts of this activity by the matrix of topographies of the corresponding sources $\mathbf{G} = [\mathbf{g}_1, ..., \mathbf{g}_L]$ and the time series $\mathbf{s}(t) = [s_1(t), ..., s_L(t)]^T$.
- $\mathbf{Bz}(t)$ — spatially incoherent brain noise representing incoherent part of the spontaneous brain activity. We also assume that these sources exhibit neither persistent (over the entire duration of the experiment), nor task-related and nor transient but task unrelated coupling. If this were not the case, such sources would be captured by the induced and coherent background activity component. Here we assume that spatially coherent interference originating from the sources outside the brain (heart artifact, noise from external equipment, metal implants) has been removed from the data by means of spatial filtering. Brain noise topographies are $\mathbf{B} = [\mathbf{b}_1, ..., \mathbf{b}_M]$, and $\mathbf{z}(t) = [z_1(t), ..., z_M(t)]^T$ are the corresponding time series. The next component models the additive sensor noise.
- $\mathbf{n}(t)$ — additive spatially-white random noise vector which we refer

to consider the data in the space of virtual sensors obtained by calculating the projection coefficients onto a subset of principal directions of the forward model matrix. The formulation presented here accommodates this point of view without any conceptual changes. The value of K corresponding to the number of sensors will then reflect the number of virtual sensors corresponding to the number of principal directions capturing a specific percentage of variance in the original forward model. Correspondingly, the forward matrices $\mathbf{A}, \mathbf{G}$ and $\mathbf{B}$ of our model will be replaced by the corresponding products with the matrix containing the principal component coordinates in the original space.

In what follows in order to avoid the trivial result caused by the activity that is phase-locked to the task onset we will be dealing with the data with removed evoked response component by subtracting its estimate. The estimate of the evoked response component $\mathbf{x}^{er}(t)$ can be efficiently done via stimulus-locked averaging. Therefore, in the rest of this paper we will exclude the evoked response component from consideration and consider the following observation model:

$$\mathbf{x}(t) = \mathbf{x}^{tot}(t) - \mathbf{x}^{er}(t) = \mathbf{Gs}(t) + \mathbf{Bz}(t) + \mathbf{n}(t) \qquad (2)$$

Brain activity recorded with MEG and EEG can be described as a non-stationary mixture of narrow-band components and is best characterized in the time-frequency domain. Let $\mathbf{X}(t,f)$, $\mathbf{S}(t,f)$, $\mathbf{B}(t,f)$ represent time-frequency transform coefficients of $\mathbf{x}(t)$, $\mathbf{s}(t)$ and $\mathbf{z}(t)$ correspondingly obtained via a linear time-frequency transform (e.g. wavelet transform, short-term Fourier transform). Our observation equation in the time-frequency domain will read as

$$\mathbf{X}(t,f) = \mathbf{GS}(t,f) + \mathbf{BZ}(t,f) + \mathbf{N}(t,f) \qquad (3)$$

2.2. Sensor-space cross-spectrum generating equation and spatial leakage

Complex-valued sensor-space cross-spectral matrix is defined as the correlation matrix of the vector of time-frequency transformed data and can be formally expressed as

$$\mathbf{C}^{XX}(t,f) = E\{\mathbf{X}(t,f)\mathbf{X}^H(t,f)\} = \Re(\mathbf{C}^{XX}(t,f)) + \mathrm{i} \cdot \Im(\mathbf{C}^{XX}(t,f)) \qquad (4)$$

In paradigms with repeated stimulus presentation, the expectation operation in (4) is approximated by the stimulus-locked averaging operation $\mathbf{C}^{XX}(t,f) \approx \frac{1}{R}\sum_{i=1}^{R}\mathbf{X}_i(t,f)\mathbf{X}_i^H(t,f)$ where $\mathbf{X}_i(t,f)$ is the time-frequency representation of the i-th trial.

By substituting the generative model (3) into the definition of the cross-spectrum (4), expanding matrix multiplications into sums of column outer products and grouping real and imaginary components, similarly to the way it was done in (Ewald et al. (2014)) we obtain:

$$\mathbf{C}^{XX}(t,f) = \boxed{\sum_{i=1}^{L}\mathbf{g}_i\mathbf{g}_i^T c_{ii}^{ss}(t,f)} + \sum_{i=1}^{L}\sum_{j=i+1}^{L}\left(\mathbf{g}_i\mathbf{g}_j^T + \mathbf{g}_j\mathbf{g}_i^T\right)\Re(c_{ij}^{ss}(t,f)) + \boxed{\sum_{i=1}^{M}\mathbf{b}_i\mathbf{b}_i^T c_{ii}^{zz}(t,f)} +$$
$$+ \mathrm{i} \cdot \left[\sum_{i=1}^{L}\sum_{j=i}^{L}\left(\mathbf{g}_i\mathbf{g}_j^T - \mathbf{g}_j\mathbf{g}_i^T\right)\Im(c_{ij}^{ss}(t,f))\right] + \mathbf{C}^{NN}(t,f) \qquad (5)$$

to as sensor noise. This noise is of non-brain origin and usually corresponds to the sensor noise. This is the last component of our generative model.

Note that our formulation presented above does not limit the number of sources N, L, M in any of the constituents of our model. Theoretically, the sources of all the components may exhaust the entire source space.

Also note that it is customary in the analysis of EEG and MEG datasets

Here $\mathbf{C}^{NN}(t,f) = E\{\mathbf{N}(t,f)\mathbf{N}^H(t,f)\}$ is a diagonal cross-spectral matrix of the spatially white additive sensor noise, c_{ij}^{ss} are the coherent activity source-space cross-spectrum values, elements of $\mathbf{C}^{ss}(t,f) = E\{\mathbf{S}(t,f)\mathbf{S}^H(t,f)\}$ that we need to estimate. Also, c_{ij}^{zz} are the elements of the source-space cross-spectral matrix of the incoherent brain noise sources $\mathbf{C}^{zz}(t,f) = E\{\mathbf{Z}(t,f)\mathbf{Z}^H(t,f)\}$.

It is important to recognize that while stimulus-locked averaging used

to compute the cross-spectrum will emphasize the task-related activity, the background networks will still contribute to the stimulus-locked cross-spectrum with a component whose proportion will not necessarily vanish as the number of trials increases.

Observe that the boxed terms in (5) depend only on the power of the sources c_{ii}^{ss} and c_{ii}^{zz} and represent the spatial-leakage effect (SL). Since c_{ii}^{ss} and c_{ii}^{zz} are real numbers and the auto-terms $\mathbf{g}_i\mathbf{g}_j^T - \mathbf{g}_j\mathbf{g}_i^T$ in the summation in the imaginary part vanish for $i = j$, the entire SL effect is present only in the real part of the cross-spectrum. As outlined in the Introduction, this very observation (Nolte et al. (2004b)) led to creation of the plethora of methods for non-invasive imaging of within frequency coupling from EEG and MEG measurements using only the imaginary part of cross-spectrum, a statistics which is free from the SL effect.

Two issues remain unaddressed by current methods. First, the summands in the imaginary part of cross-spectrum are modulated by the imaginary part of the source-space cross-spectrum $\Im(c_{ij}(t,f))$. By construction, the imaginary part has maximum sensitivity to $90°$ phase difference of the coupled time series. Therefore, the coherent source pairs with close to zero mean phase difference contribute to the imaginary part of the sensor-space cross-spectrum with low SNR. Second, while the real part of the sensor space cross-spectrum will have maximal contributions from any true zero-phase (or instantaneous) interactions, it is also contaminated by the spatial leakage effect that adversely affects the resultant SNR.

One possible way to tackle this problem lies in attempting to selectively and significantly suppress the contribution of the SL to the real part of the sensor-space cross-spectrum.

2.3. PSIICOS projection

The main step of the proposed method is a novel projection procedure operating in the space of sensor signals cross-spectral matrices, which is the key manipulation we use to circumvent the spatial leakage effect. In order to design such a projector we will start with two crucial observations outlined below. Additional related details can be found in Appendix.

2.3.1. Vectorized cross-spectrum

Consider the vectorized form of the cross-spectral matrix (5). For compactness we denote $\mathbf{q}_{ij} = vec\left(\mathbf{g}_i\mathbf{g}_j^T\right) = \mathbf{g}_j \otimes \mathbf{g}_i$ and $\mathbf{h}_{ii} = vec(\mathbf{b}_i\mathbf{b}_i^T) = \mathbf{b}_i \otimes \mathbf{b}_i$ and obtain:

cross-spectrum modulates power in the $S^\Re = span(\mathbf{q}_{ij} + \mathbf{q}_{ji}), i \neq j, (i,j) = (1, ..., M, 1, ..., M), i > j$ subspace and the imaginary part of the source-space cross-spectrum projects into $S^\Im = span(\mathbf{q}_{ij} - \mathbf{q}_{ji}), i \neq j, (i,j) = (1, ..., M, 1, ..., M)$ subspace of the sensor-space cross-spectrum, see also (Ewald et al. (2014)). In what follows we will refer to $S^\Re$ and $S^\Im$ as real and imaginary true coherence subspaces respectively.

2.3.3. Building and applying the projector

In (6) we assume L sources of coherent brain activity. L is likely to be much smaller than M: i.e. task-induced source activities are going to be fewer in number than brain noise generators. The brain noise term $\sum_{i=1}^{M} \mathbf{h}_{ii} c_{ii}^{zz}(t,f)$ collects a relatively large population of sources whose distribution varies over the course of the experiment, the longer the experiment the greater M and the grid of brain-noise sources may theoretically cover the entire cortex. The SL effect caused by these task unrelated sources masks the contributions from the genuinely coherent task-related and task unrelated pairs. An efficient way to address this issue lies in designing a projector into the subspace orthogonal to the spatial leakage subspace S^{SL} of *all* potential sources. To do so

- Start from the whole head (cortex) forward model matrix $\mathbf{G} = \{\mathbf{g}_{ij}\}$, $i = 1, ..., K, j = 1, ..., D$ corresponding to all D grid nodes containing sources with fixed orientation (see Appendix for extension to arbitrary source orientation case). First form the $K^2 \times D$ matrix $\mathbf{F}$ of SL topographies $\mathbf{q}_{ii} = vec(\mathbf{g}_i\mathbf{g}_i^T), i = 1, ..., D$:

$$\mathbf{F} = [\mathbf{q}_{11}, \mathbf{q}_{22}, ..., \mathbf{q}_{DD}] \tag{7}$$

- Form projection matrix away from the SL subspace as $\mathbf{P} = \mathbf{I} - \mathbf{U}_R\mathbf{U}_R^T$ where $\mathbf{U}_R = [\mathbf{u}_1, \mathbf{u}_2, ..., \mathbf{u}_R]$ is a matrix of the first R left singular vectors of $\mathbf{F}$ spanning the most powerful R-dimensional subspace of S^{SL}. The selection of the rank R of the projection operator is discussed below.
- Use projection operator $\mathbf{P}$ to suppress the contribution of the SL effect to the sensor-space cross-spectrum $vec(\mathbf{C}^{XX})(t,f)$ as follows:

$$vec(\mathbf{C}^{XX})^{\perp SL}(t,f) = \mathbf{P}vec(\mathbf{C}^{XX})(t,f) \tag{8}$$

Since the outlined PSIICOS projection procedure will affect the $S^\Re$ as well we need to achieve some balance between the extent to which we

$$vec\left(\mathbf{C}^{XX}\right)(t,f) = \boxed{\sum_{i=1}^{L} \mathbf{q}_{ii} c_{ii}^{ss}(t,f)} + \sum_{i=1}^{L}\sum_{j=i+1}^{L}(\mathbf{q}_{ij} + \mathbf{q}_{ji})\Re(c_{ij}^{ss}(t,f)) + \boxed{\sum_{i=1}^{M} \mathbf{h}_{ii} c_{ii}^{zz}(t,f)} +$$
$$+ i \cdot \left[\sum_{i=1}^{L}\sum_{j=i}^{L}(\mathbf{q}_{ij} - \mathbf{q}_{ji})\Im(c_{ij}^{ss}(t,f))\right] + vec\left(\mathbf{C}^{NN}\right)(t,f) \tag{6}$$

Now, all additive elements of this equation are $K^2 \times 1$ vectors obtained by stacking all the columns of the corresponding $K \times K$ matrices, where K is the number of sensors.

2.3.2. Spatial structure and spatial leakage component subspace

In the above equation (6) the framed terms $\sum_{i=1}^{L} \mathbf{q}_{ii} c_{ii}^{ss}(t,f)$ and $\sum_{i=1}^{M} \mathbf{h}_{ii} c_{ii}^{zz}(t,f)$ represent spatial leakage (SL) of source power into the real part of the sensor-space cross-spectrum. Operating in linear algebra terms we can say that the spatial leakage subspace S^{SL} of the vectorized cross-spectrum is spanned by spatial leakage topographies $\mathbf{q}_{ii}, i = 1, ..., L$ and $\mathbf{h}_{ii}, i = 1, ..., M$. Similarly note that the real-part of the source space

mitigate the SL and how much the power in the $S^\Re$ subspace is preserved. We manage this trade-off by adjusting the choice of R, the rank of the projection operation. The extent to which the spatial leakage component is suppressed depends solely on the geometric properties of the head-sensor array system. The informed choice of projection rank parameter R used in Step 3 above can be determined considering the changes of suppression power in the SL and $S^\Re$ subspaces as a function of projection rank as shown in Fig. 14 of the Appendix. Since the two subspaces overlap and because the PSIICOS projector is built using the SVD procedure that concentrates most power in the first components, the PSIICOS projection based on the lower rank values will primarily target the

SL components and the rate of decay of power in the SL subspace will be higher than that in the $S^{\Re}$ subspace. Importantly, for some specific value of projection rank R^* the two curves become nearly parallel which corresponds to the equal decay rate meaning that the PSIICOS projection empty power from the SL and $S^{\Re}$ subspaces to the equal extent, see Fig. 14 a). This critical value of projection rank can be better appreciated from the plot in Fig. 14 b) where we show the mean difference between the suppression factors of SL and $S^{\Re}$ components as a function of PSIICOS projection rank for the three different virtual sensor space dimensions. It can be seen that when operating in the 30-dimensional virtual sensor space the difference of suppression factors exhibits a clear maximum around for $R^* = 125$. This low rank of VS is not recommended, however, for its relatively low difference in the suppression of power in $S^{\Re}$ and SL subspaces. According to these graphs, operating in 60 dimensional VS space we should choose R^* in the 150–200 range to achieve the maximum suppression difference. Using 80 VSs, we should opt for R^* in 200–250 range. Our experiments with analysis of synthetic and real data show that variations of the projection rank parameter within 20% of the optimal value do not qualitatively affect the results. The optimal value of R^* will experience moderate variability across different types of MEG systems. Therefore, for better performance, the value of R can be obtained via similar analysis.

Note, that the proposed procedure does not require an estimation of source power from the particular dataset at hands. We compute $\mathbf{P}$ based on the entire set of source-space elements (as represented in the forward model matrix $\mathbf{G}$) and therefore we have addressed the SL contribution of all sources including brain noise generators as it is expressed in the observation model (2). As a consequence, the selection of R^* for the $\mathbf{P}$ operator does not depend on the measurements and is uniquely determined by the forward model.

Although in what follows we will refer to the matrix $\mathbf{C}^{XX \perp SL}(t,f)$ as *PSIICOS projected cross-spectrum* or *SL debiased cross-spectrum* it is important to recognize that $\mathbf{C}^{XX \perp SL}(t,f)$ is not a proper cross-spectral matrix. It is no longer positive definite (due to suppression of the diagonal terms) and no normalized measure can be calculated from this projected matrix. If normalization is needed, however, it is in principle possible to do so using source power estimates c_{ii} from the original matrix $\mathbf{C}^{XX}(t,f)$.

2.4. Phase shift independent estimation of the source-space cross-spectrum

We used equations (7) and (8) in order to derive the projector into the subspace orthogonal to S^{SL}. Once we have this projector we can return to the much more compact equation (5) and after applying the projection operation write

$$vec\left(\mathbf{C}^\perp\right)(t,f) = \sum_{i=1}^{L} \sum_{j=1}^{L} \mathbf{q}_{ij}^\perp c_{ij}^{ss}(t,f) + \varepsilon(t,f) \qquad (9)$$

In the above $\mathbf{q}_{ij}^\perp = \mathbf{P}\mathbf{q}_{ij}$ are the projected interaction topography vectors and $\varepsilon(t,f)$ is the noise term encapsulating the leftovers of the spatial leakage component from the sources of interest and incoherent brain-noise that survived the rank-truncated projection away from the SL subspace:

$$\varepsilon(t,f) = \mathbf{P}\sum_{i=1}^{M}\mathbf{h}_{ii}c_{ii}^{zz}(t,f) + \mathbf{P}\sum_{i=1}^{M}\mathbf{q}_{ii}c_{ii}^{ss}(t,f) + \mathbf{P}\mathbf{C}^{NN}(t,f) \qquad (10)$$

Consideration of the vectorized form of the cross-spectral matrix allowed us to construct the efficient projection procedure for suppressing the undesirable SL components in the real-part of the sensor-space cross-spectrum. Additional benefit of the vectorization based view is that it allows us to appreciate the fact that equation (9) is simply a linear regression equation, similar to the one we use when solving the source estimation problem, but formulated in the product space of sensor signals. Instead of source activation time-series (as in (2)) or their time-frequency profiles in the regular equation the unknown regression coefficients in equation (9) are the time-frequency profiles of the source-space cross-spectral coefficients. Now we can estimate $c_{ij}^{ss}(t,f)$ with a plethora of methods developed for solving the classical inverse problem in MEG and EEG. In this work in order to demonstrate the performance of the suggested projection procedure and perform ROC analysis based on the simulated source-space ground truth we decided to choose the inverse mapping procedure based on projecting the data onto the normalized interaction topography vectors.

We perform a simple scan by computing the inner product of the corresponding projected interaction topographies $\mathbf{q}_{ij}^\perp$ at each time-frequency slice of the vectorized and projected cross-spectrum matrix $vec(\mathbf{C}^\perp(t,f))$ to obtain $\rho_{ij}(t) = \langle \mathbf{q}_{ij}^{\perp \max}/\left\|\mathbf{q}_{ij}^{\perp \max}\right\|^2, vec(\mathbf{C}^\perp(t,f))\rangle$.

The quantity $\rho_{ij}(t)$ uses $\mathbf{q}_{ij}^{\perp \max}$ interaction topography maximizing the $\rho_{ij}(t)$ over all possible orientations of the i-th and the j-th source. Based on the value of $\rho_{ij}(t)$ we can judge about the presence of a pair of interacting sources at the coordinates corresponding to the i-th and j-th node at time instance t. To ensure the stability of the observed distribution of ρ_{ij} the bootstrap resampling procedure adopted from Darvas et al. (2005) described in section 3 can be used. Block *Est. source-space cross-spectrum* in Fig. 1 illustrates this scanning procedure. The SL-free sensor-space cross-spectrum is projected onto appropriately normalized PSIICOS projected interacting topography vectors ($\mathbf{q}_{ij}^\perp = \mathbf{P}\left(\mathbf{g}_j \otimes \mathbf{g}_i\right)$) to yield an estimate of the source-space cross-spectral coefficient, much like dipolar time series are obtained by projecting the data onto the normalized dipole topographies.

The proposed approach for calculating the source-space connectivity values by a simple regression of the SL-debiased cross-spectrum onto the elementary network topographies is alternative to the most commonly used two-step procedure where first, source time series are estimated using either MNE or a beamforming technique (such as LCMV) and then a connectivity measure is calculated. Note, however, that the proposed regression procedure is optimal only in case $\varepsilon(t,f)$ is spatially white and the active network topographies $\mathbf{q}_{ij}^\perp$ are orthogonal. Therefore, in order to take full advantage here more sophisticated source estimation methods developed in the field should be adopted to operate in the K^2 dimensional space of elementary network topographies.

The overall data processing flow is illustrated in panel c) of Fig. 1. In addition to the standard steps, it includes building the PSIICOS projector and applying it to the sensor-space cross-spectrum. The same projection is applied to the topographies of elementary networks to be used in the source-space scan to obtain the estimates of the source-space cross-spectral coefficients.

2.5. Graphical illustration of the algorithm

The diagram in panel a) of Fig. 1 illustrates the idea behind the proposed projection operation by showing the relationship between the vector components that comprise sensor-space cross-spectrum. It is straightforward to show that $S^{\Re} \perp S^{\Im}$, $S^{\Im} \perp S^{SL}$ and that $S^{\Re} \cap S^{SL} \neq \varnothing$. Physically, the intersection of $S^{\Re}$ and S^{SL} is primarily occupied by the contributions from the real-part of cross-spectrum of functionally coupled sources located close to each other whose activations can be characterized by zero or close to zero mean phase difference.

On panel b) of Fig. 1 we illustrate the proposed projection procedure and the way it affects the original cross-spectrum $\mathbf{C}^{XX}$. $\mathbf{C}^{XX}$ can be decomposed into the two orthogonal real and imaginary components, $\Re(\mathbf{C}^{XX})$ and $\Im(\mathbf{C}^{XX})$. The projection operation leaves the imaginary component of the original cross-spectrum intact. In turn, the real component of the sensor-space cross-spectrum, $\Re(\mathbf{C}^{XX})$, can be decomposed into the spatial leakage component and its complement $\mathbf{P}\Re(\mathbf{C}^{XX})$ that belongs to the real true coupling subspace $S^{\Re}$. The aim of the

(a) Venn diagram for interrelation of subspaces in the sensor space cross-spectrum.

(b) Vector diagram of PSI-ICOS projection
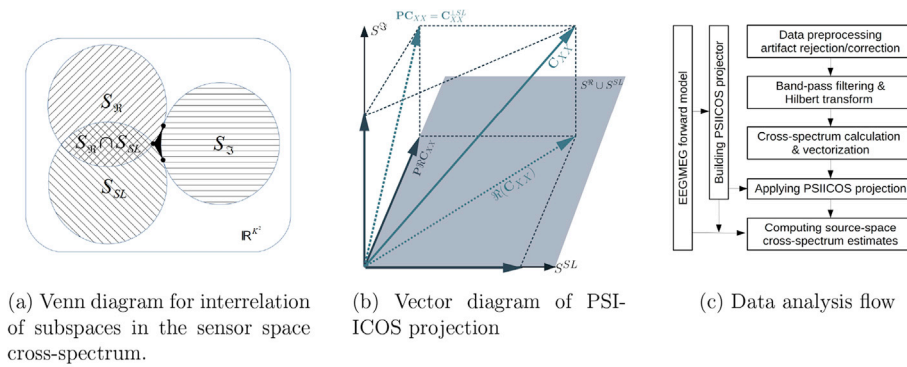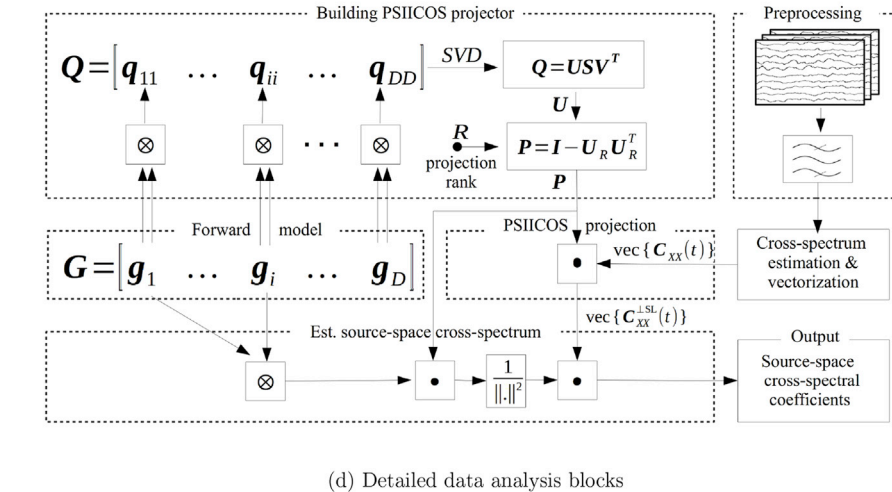
(c) Data analysis flow

Fig. 1. a) — The spatial leakage subspace and the real part subspace overlap and are orthogonal to the subspace of the imaginary component of the cross-spectrum. The intersection of the two former subspaces contains contributions from the spatial leakage and from the real-part of the non-diagonal cross-spectrum elements for the sources located close to each other whose activity can be characterized by a zero or close to zero value of mean phase difference. Note that the three subspaces have common to all of them null vector. However, this null vector is the only element of $S^\Re \cup S^\Im$. To reflect this fact we highlighted the center of the diagram that marks the null-vector common to all three subspaces. b) — The effect of the proposed projection procedure on the original cross-spectral vector $\mathbf{C}^{XX}$. The dashed red arrow represents the result of the projection of the real part of the original cross-spectrum into the subspace orthogonal to the spatial leakage subspace. It is important to recognize that S^{SL} and $S^\Re$ are not orthogonal and there is always a trade-off between the extent to which the S^{SL} power is canceled and the degree of suppression of the signals in $S^\Re$. The dashed red arrow represents the projected complex cross-spectrum that can be represented as a sum of the imaginary part that is left intact by the projection and the real part of the original cross-spectrum $\mathbf{C}^{XX}$ projected into the complement of the S^{SL}

c) General view of the processing flow that in addition to the standard steps includes building the PSIICOS projector and applying it to the sensor-space cross-spectrum. The same projection is applied to the topographies of elementary networks to be used in the source-space scan that yields the estimates of the source-space cross-spectral coefficients. d) The main component of the proposed method is PSIICOS projection that is based on an estimate of the spatial leakage subspace using the vectorized outer products of all source topography vectors, $vec\{\mathbf{g}_i\mathbf{g}_i^T\} = \mathbf{g}_i \otimes \mathbf{g}_i$, $i = 1$, $\dots,D$. The projection is calculated using the subset of R left singular vectors and applied to the vectorized estimate of the band-specific sensor space cross-spectrum. Then, in order to obtain the estimates of the source-space cross-spectrum elements, the SL-free sensor-space cross-spectrum is projected onto appropriately normalized PSIICOS projected interacting topography vectors calculated as $\mathbf{q}_{ij}^\perp = \mathbf{P}(\mathbf{g}_i \otimes \mathbf{g}_j)$, $(i,j) = (1,\dots,M, 1,\dots,M)$, $i > j$ to yield and estimate of the source-space cross-spectral coefficient.

(d) Detailed data analysis blocks

projection is to remove from the real part of the cross-spectrum vector the contribution lying in the spatial leakage subspace S^{SL}.

The real true coupling $S^\Re$ and the spatial leakage subspaces S^{SL} are not orthogonal. Therefore, while the projection operation dominantly targets the spatial-leakage components it nevertheless also affects the vectors in the real true coupling subspace. As a result, we obtain a debiased, predominantly SL-free cross-spectrum $\mathbf{PC}^{XX}$ that represents all range of coupled sources with somewhat diminished contribution from those located close to each other and with zero or near-zero phase coupling (since closely located sources generally have correlated topographies, their real-part contribution to the cross-spectrum $\mathbf{C}^{XX}$ to a larger extent resembles that of the signal leakage subspace; therefore the projection operator will affect the real-part contribution of the close-by sources the most).

Graphical illustration of the steps aimed at building the PSIICOS projector are outlined in the *Building PSIICOS projector* block of the diagram depicted in panel d) of Fig. 1. It is based on an estimate of the spatial leakage subspace using the vectorized outer products of all source topography vectors, $vec\{\mathbf{g}_i\mathbf{g}_i^T\} = \mathbf{g}_i \otimes \mathbf{g}_i$, $i = (1,\dots,D)$. The projection is calculated using the subset of R left singular vectors and applied to the

vectorized estimate of the band-specific sensor space cross-spectrum.

3. Bootstrap resampling for reproducibility testing

In order to check for stability of the observed solutions a bootstrap procedure similar to that described in Darvas et al. (2005) can be used. We first generate B bootstrap cross-spectral time series (CT) obtained by averaging epochs whose indexes are generated by the uniform sampling with replacement procedure. Then on each bootstrap iteration, a small number m of edges corresponding to the networks with the highest source space scan values are grouped into several clusters according to the Spatial Pairwise Clustering (SPC) procedure from Zalesky et al. (2012). For each identified cluster a centroid connection is calculated by within cluster averaging of the beginning and end coordinates of the line segments with properly picked mutual orientations. These cluster centroids characterized by a line segment terminated by two points on the cortical surface, are retained from each of the B bootstrap iterations and collected. In order to quantify the spatial spread of thus collected cluster centroids, we define the distance between a pair of connections as the minimal sum of Euclidean distances between their terminal points, where

the minimum is chosen out of the two values corresponding to the two possible mutual orientations of the pair of connections. Finally, according to the distance function described above, we define the reproducibility index η as reciprocal of the averaged across all B resamples distance from a connection to its nearest neighbor.

4. Monte-Carlo simulations

In order to compare the proposed technique against other relevant methods for detection of coupling in source space we ran a set of realistic simulation studies. We used Freesurfer-extracted cortical surface with 15000 vertices and calculated the high-resolution forward model matrix $\mathbf{G}^{HR}$ with two columns per vertex corresponding to the two orthogonally oriented dipoles in the 2-D space orthogonal to the right singular vector corresponding to the smallest singular value of the original $K \times 3$ forward model matrix of the vertex. We simulated event-related field (ERF) experiment data with 100 repetitions (epochs) of the task. The induced activity of coupled sources was modeled with two 10 Hz sinusoidal functions with random phase w.r.t. stimulus onset but probabilistically connected via phase difference term $\delta\phi$ sampled from a random distribution taking values in the $[-\pi/4, \pi/4]$ range.

We modeled brain noise with $Q = 1000$ spatially coherent, task-unrelated cerebral sources whose locations and time series varied with each epoch. Source locations matched nodes of the high-resolution cortical surface (15000 vertices). The activation time series were narrow-band signals obtained via zero-phase filtering of realizations of Gaussian (pseudo)random process by the fifth order band-pass IIR filters in the bands corresponding to theta (4–7 Hz), alpha (8–12 Hz), beta (15–30 Hz) and gamma (30–50 Hz, 50–70 Hz) activity. Their relative contributions were scaled in accordance with $1/f$ characteristic of the realistic MEG spectrum. We scaled the brain noise components to match typical signal-to-noise ratio of real-life recordings. To project these sources into the sensor space, the corresponding columns of $\mathbf{G}^{HR}$ were linearly combined to represent the orthogonally oriented dipole in each of the Q chosen nodes. We simulated 100 epoch ERF data and for each epoch a new randomly picked set of noisy sources was chosen and new noisy time series with approximately $1/f$ spectrum were generated. We defined the SNR in our simulated data in the sensor space as the ratio of Frobenius norms of data matrices of the induced and brain noise components filtered in the band of interest (8–12 Hz).

We computed frequency specific sensor-space cross-spectral matrix by averaging over epochs the outer products of channel time series Fourier coefficients that fall in the 8–12 Hz frequency range. In order to simulate the real-life circumstances when source coordinates do not necessarily match a vertex in a mesh, we used the high-resolution cortex only to simulate the data. We employed the 10 times sparser representation of the cortex with 1503 nodes for construction of the PSIICOS projection operator and for the source-space elementary networks scan according to the workflow in Fig. 1.

As a threshold-free performance metrics, we used the Precision-Recall (PR) and Receiver Operating Characteristics (ROC) curves. The Precision-Recall metrics suites well the situation when we have a small number of true positives and the number of choices is large. The ROC curve, *sensitivity* vs *1 - specificity* plot, in this case is informative only for extremely high specificity values. More details and the definition of these two metrics can be found in section 8.4 of the Appendix.

Thus, for each MC trial, we calculated a ROC curve then averaged these ROC curves over the entire set of 1000 Monte-Carlo trials. We considered two different SNR values ($SNR_1 = 1.0$ and $SNR_2 = 0.2$). Since the proposed method is designed to achieve uniform performance for all values of the phase-lag between the coupled sources we have performed separate studies for two different mean phase-lag values: $\phi = \pi/2 - \pi/20$ and $\phi = \pi/20$ radians. We have also explored the performance for a grid of mean phase lags.

We first used only one pair of interacting sources placed at random

locations on the high-resolution cortex at each MC trial. To simulate the transient nature of such a network within each trial we modulated this synchronized activity by a window function $w(t)$ that coincided with the one corresponding to Simulated profile 1 as depicted in Fig. 2 and activated the network only during the first half of each trial. At each MC trial, we generated a 100 epoch dataset with a fixed spatial configuration of target sources and varying from epoch to epoch constellation of brain noise sources. For detection of networks, we used the entire trial time range to mimic the situation when we don't know the interval during which the network is active.

In the second study, we simulated the data with three concurrently active networks having a spatial and temporal structure as illustrated in Fig. 2. The main challenge here was to resolve the three networks with the overlapping windows of activity.

We compared PSIICOS against three other methods for detection of synchronous sources. The first method we compare PSIICOS against is the Dynamic Imaging of Coherent Sources (DICS) Gross et al. (2001). The method consists in applying a frequency domain beamformer to the Fourier coefficients of the multichannel sensor-space data followed by computing the coherence values of thus extracted Fourier domain representation of the source space signals. For each pair of sources, the largest eigenvalue of the elementary source-space cross-spectral matrix normalized by the source power estimates is then used to quantify the coherence between a pair of sources. To exclude spatial leakage effects, we used a modified version of this technique where we only exploit the imaginary part of the source-space cross-spectral matrix. This modified DICS approach called further iDICS serves as the second method to which we compare PSIICOS. The third method we use in our comparative study of PSIICOS is Geometric Correction Scheme (GCS) approach developed by Wens et al. (2015). This method is conceptually most closely related to the technique proposed here and suggests to apply a model based
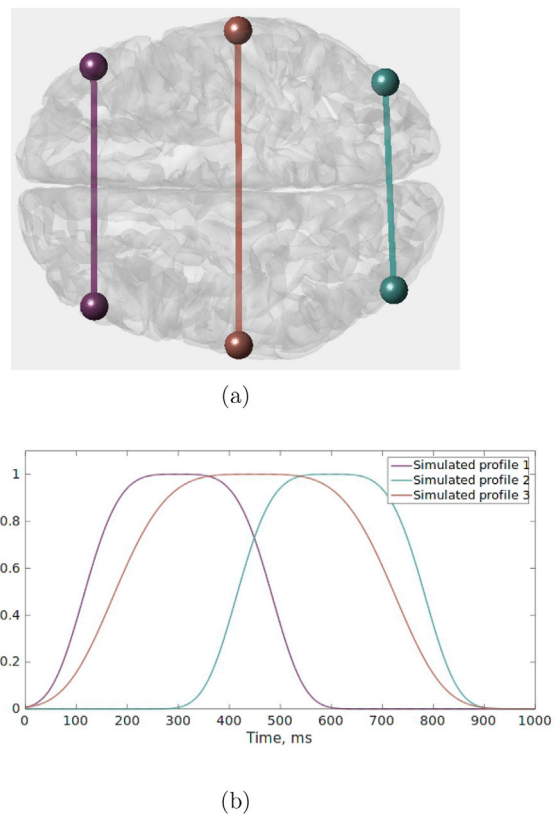

(a)

(b)

Fig. 2. Three simulated pairs of coupled sources. a) — the spatial topography of the simulated sources, b) — temporal profiles of coupling for each of the three pairs of sources.

geometric transformation to the second source data to remove the spatial leakage effect from the first source. As in the original paper, we use minimum norm estimate (MNE) and exploit known brain-noise covariance matrix, the information not required by PSIICOS.

5. Real data analysis

We applied the proposed technique to real MEG data that were acquired in a mental rotation study (De Lange et al., 2008) from which single-subject data were made publicly available at Biomag 2010 Data Analysis Competition. During the recording, the subject had to report by pressing one of two buttons, the laterality corresponding to the hand drawing displayed on the screen. The displayed drawings of the hands were isometric images of a wrist rotated at different angles with respect to the observer (subject). The dataset contained 800 trials with randomized rotations and laterality split into 5 blocks. Each trial comprised the following sequence of events: fixations cross (3 s), hand drawing displayed until the decision was made, fixation cross (0.5 s) with color indicating the feedback (red — wrong, green — correct). Subjects spent on average 70 min in the MEG scanner.

During the experiment, brain activity was recorded using the whole-head MEG with 151 axial gradiometers (VSM/CTF Systems, Port Coquitlam, British Columbia, Canada). The analog signals were low-pass filtered at 300 Hz and sampled at 1200 Hz. After bad segments removal and artifact rejection, the total of 259 epochs corresponding to the stimuli displaying images of the left hand remained for the further analyses. The trials were of variable length (from 1.52 to 2.08 s) and were realigned so each epoch started 0.5 s prior to the image appearance on the screen. We analyzed 1 s of data past the stimulus.

In order to scan through the range of frequencies we considered the following standard bands: theta (4–8 Hz), alpha (8–12 Hz), beta (16–24 Hz), lower gamma (30–60 Hz) and the higher gamma band (65–85 Hz) (e.g. Moran et al. (2010); Caetano et al. (2007); Casanova et al. (2017); Lee et al. (2007)).

We first applied the zero-phase FIR filtering to isolate the frequency bins. Then, by averaging across epochs of the outer products of Hilbert-transformed data we computed time-resolved cross-spectral tensors and reshaped them to obtain $K^2 \times T$ vectorized cross-spectral matrices of the $K = 151$ sensor signals. Next, we applied the PSIICOS projection, corresponding to the rank $R = 150$ which was determined based on the considerations outlined in section 2.3. Importantly, R values ranging from 100 to 250 were explored with little impact on the overall results.

We then analyzed separately real and imaginary parts of the vectorized time-resolved cross-spectrum. Instead of simple averaging over time-axis, in order to discover the spatial structure, we first performed singular value decomposition (SVD) of the real and imaginary parts of the PSIICOS-projected vectorized time-resolved cross-spectrum. We then performed source space scan for each of the first two left singular vectors of the real and imaginary parts of the PSIICOS-projected cross-spectrum using the dense source-space grid with 15000 vertices.

In order to check for stability of the observed solutions, we used the bootstrap procedure described in Section 3 with $m = 30$ and $B = 100$ and plotted the reproducibility index η. The networks are then shown only for the reproducible bands and components with the edges whose ends correspond to the coupled cortical regions. The edges whose nodes appeared to be closer than 1 cm apart were plotted in the same color. Also, for each reproducible component, we plot its temporal profile as the right singular vector of the time-resolved cross-spectrum.

6. Results

6.1. Effect of projection on the source space cross-spectrum components

As evident from the diagram in Fig. 1 because of the orthogonality of $S^{\Im}$ and S^{SL} subspaces the projection operation does not alter the imaginary part of the cross-spectrum. Conversely, the components from $S^{\Re}$ subspace carrying information about the real part of source-space cross-spectrum do get affected by such a projection operation and by removing the SL variance from the sensor-space cross-spectrum we will inevitably remove some part of the variance modulated by the real part of the source space cross-spectrum non-diagonal elements. The performance and usability of the proposed PSIICOS projection in suppressing the spatial leakage contribution to the real part of the sensor space cross-spectrum critically depends on the following two factors:

- The PSIICOS projection should maximally suppress the power of components in the SL subspace while minimally affecting that in the true real coherence subspace.
- As it is the case for all inverse solution frameworks the PSIICOS projection heavily depends on the forward model and therefore, the inevitable inaccuracies of the forward model encountered in real-life (Mosher et al. (1999)) will adversely affect the performance of the proposed method. Reasonable errors in forward modeling should lead to only slight deterioration of performance.

The extent to which these desired properties hold depends on the phenomenological characteristics of the sensor array and magnetic field topographies produced by the brain sources. In this section we describe numerical simulations addressing these issues.

Clearly, the attenuation of the variance in the $S^{\Re}$ subspace is most pronounced for sources with correlated topographies. To explore the dependence of attenuation on the correlation coefficient between the topographies of the coupled sources for each combination of network node indexes i and j ($i \neq j$) we calculated the norms of the product-space topographies $vec(\mathbf{g}_i\mathbf{g}_i^T + \mathbf{g}_j\mathbf{g}_j^T)$, $vec(\mathbf{g}_i\mathbf{g}_j^T + \mathbf{g}_j\mathbf{g}_i^T)$ and $vec(\mathbf{g}_i\mathbf{g}_j^T - \mathbf{g}_j\mathbf{g}_i^T)$ spanning the three subspaces S^{SL}, $S^{\Im}$ and $S^{\Re}$ of the sensor-space cross-spectrum, see Fig. 1. We did so before the projection and after the projection operation and presented the results in Fig. 3 using the scatter plot. For each two-node network with nodes in the i-th and the j-th locations of the cortical surface, we plot three points color-coded using the three different (red, blue, yellow) palettes. The gradations of the blue color are used to depict the norm of the product-space topography vector $\mathbf{q}_{ij} + \mathbf{q}_{ji}$ spanning the $S^{\Re}$ subspace of the sensor-space cross-spectrum. The gradations of the red color are used to depict the norm of the product-space topography vector $\mathbf{q}_{ij} - \mathbf{q}_{ji}$ spanning the $S^{\Im}$ subspace of the sensor-space cross-spectrum. Finally, the gradations of the yellow color are used to depict the norm of the product-space topography vector $\mathbf{q}_{ii} + \mathbf{q}_{jj}$ spanning the S^{SL} subspace of the sensor-space cross-spectrum under the assumption of equal power of the i-th and j-th source. The position of each colored point along the x-axis for panels a), b) is determined by the correlation coefficient of topographies $\mathbf{g}_i$ and $\mathbf{g}_j$ of the dipolar sources comprising the elementary network. We have also plotted the same data but used source grid node distance for the x-axis, see Fig. 3. Color saturation reflects the density of the scattered points.

As we can see from the diagram on panels a) and c) of Fig. 3 before the projection operation the SL component (yellow) dominates the sensor space cross-spectrum. After applying the described projection operation of rank 500 (panels b) and d)) we can observe that the significant reduction in the SL component power for all values of the dipole topographies correlation coefficient. Because the S^{SL} and $S^{\Re}$ subspaces intersect the projection procedure also reduces the power in the $S^{\Re}$ subspace as it can be seen by comparing the blue scatter between s the left and the right panels. However, the reduction in the norm of the product-space topography vectors spanning $S^{\Re}$ is significantly less than the attenuation suffered by the SL subspace topography vectors.

In Appendix section 8.3 we explored the effect of forward model inaccuracies on the performance of the proposed projection procedure. It turns out that while the inaccuracies in the forward model do cause deterioration of the performance of the proposed projection scheme, for
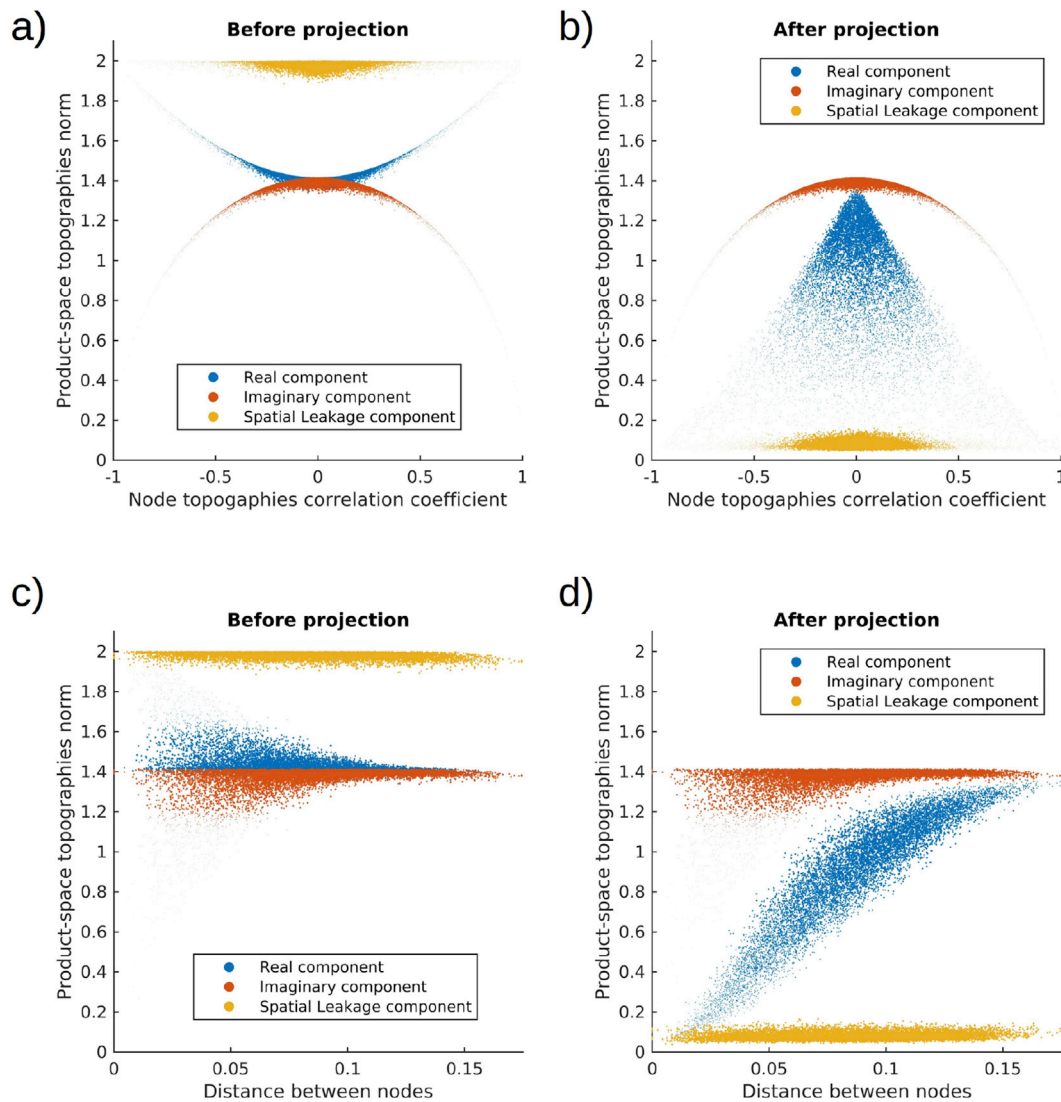
Fig. 3. Product-space topography norms for the three subspaces of the sensor-space cross-spectrum before and after the PSIICOS projection as a function of the correlation coefficient of coupled nodes source topographies (panels a) and b)) and the distance between the pair of elementary network nodes (panels c) and d)). Before the projection (panels a), c)) the sensor-space cross-spectrum is dominated by the source power component (yellow). After the projection (panels b), d)) the manifestation of the source power on the sensors gets reduced by more than a factor of 25 on average. We are also witnessing the inevitable but significantly less dramatic attenuation (1.6 in the mean value) of the real-component product-space topographies.

typical MEG forward model noise levels of 10% (Mosher et al. (1999)) the projection yields almost the same value of the SL power attenuation and only about 20% of the additional decrease in the $S^{\Re}$ subspace variance.

6.2. Comparative performance simulation study

In this section, we will describe our results comparing the proposed PSIICOS technique against three other methods outlined in Section 4 for detection of synchronous sources: DICS, iDICS and GCS.

6.2.1. Monte-Carlo study of receiver operating characteristics

To quantify the putative improvement in detection characteristics achieved by PSIICOS for various spatial network configurations, we performed a Monte-Carlo study according to the principles described in section 4.

As we can see from Fig. 4 for each of the simulation conditions PSIICOS consistently outperforms the other methods and allows achieving reasonable performance invariant to the phase lag value. As judged by the ROC curve for mean phase lag of $\phi = \pi/2 - \pi/20$ the iDICS

delivers performance comparable to that of PSIICOS. For $\phi = \pi/20$ iDICS fails to adequately detect the networks due to significantly decreased SNR of representation of nearly zero-phase lag coupling in the imaginary part of the cross-spectrum. The MNE GCS technique performs better than the DICS approach for the high SNR case, however, both of the techniques fail to deliver a reasonable performance in the low SNR case. At the same time the PSIICOS technique manages to retain the performance for both SNR values. The reason for such an improved performance lies in the use of the proposed projection operation that frees the real part of the cross-spectrum from the undesired SL component leaving only the component modulated by the real part of the cross-spectral coefficient of the two sources. As outlined earlier, for near zero mean phase lag this very component captures the information about the coupling and PSII-COS is able to detect it.

In the lower SNR case, the greater gap between PSIICOS's performance for two different mean phase lag values can be due to the presence in MC trials of networks with nodes located close to each other so that the real part of the real-interaction term gets significantly affected by the projection operation, see Fig. 14. The other techniques, however, practically stop operating under these conditions for nearly instantaneous
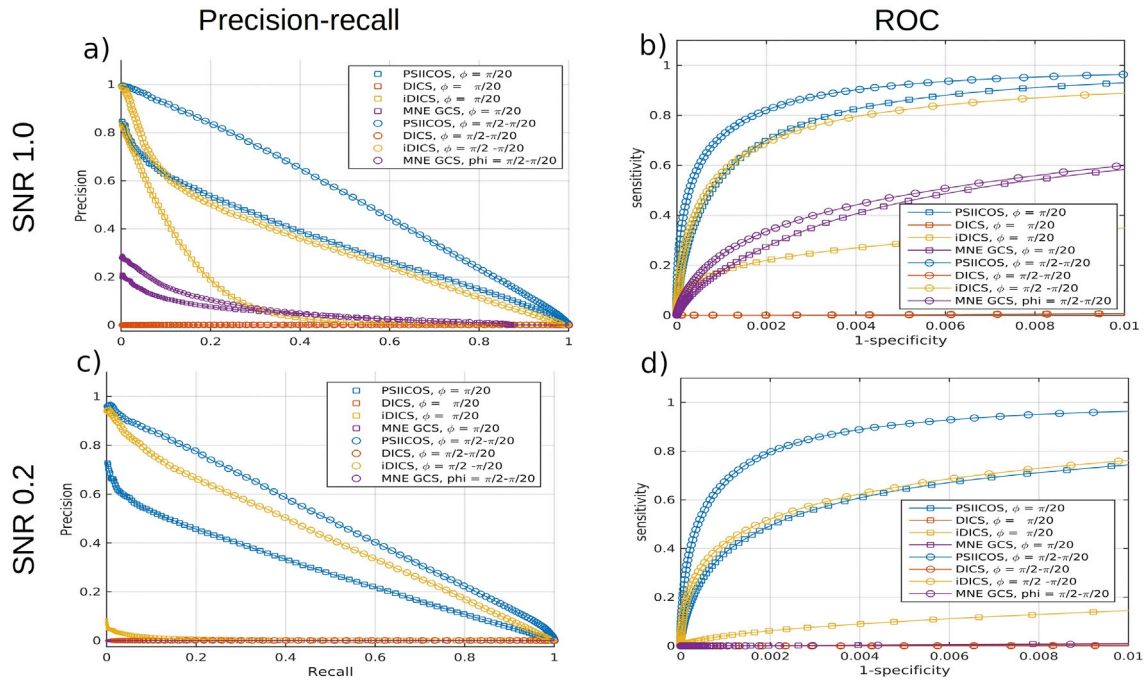
Fig. 4. Precision-recall (a,c) and ROC (b,d) curves comparing the network detection performance PSIICOS vs DICS, iDICS and GCS MNE techniques for two different SNR values based on 1000 Monte-Carlo trials.
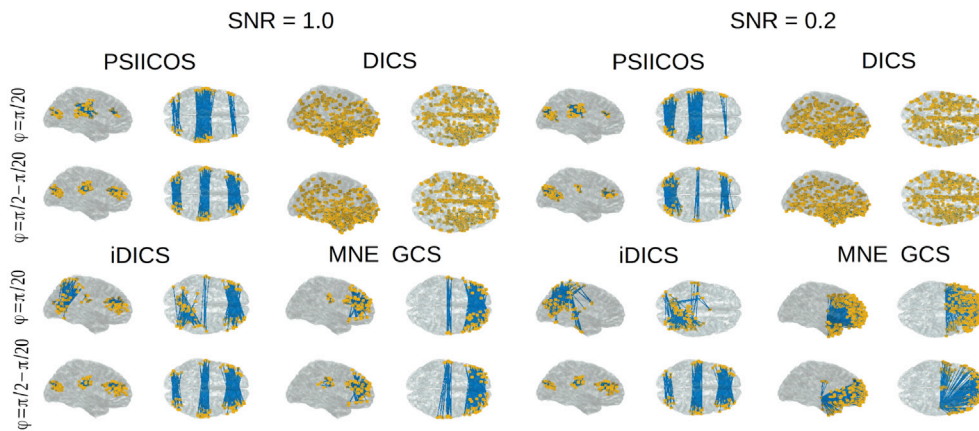

Fig. 5. Spatial structure of source-space scan for the simulated data depicting top 0.1% of connections with the highest value of the source-space connectivity statistic for PSII-COS and three other methods. As one can see only the PSIICOS technique retains reasonable performance across the whole range of the studied conditions. Consistent with our previous results the iDICS technique performance nearly pars that of PSIICOS in the close to $\pi/2$ phase lag case. The MNE GCS technique for the high SNR case quite reliably picks the two frontal networks for both values of the mean phase lag but completely stops operating for the low SNR and near zero phase lag case. For the close to $\pi/2$ phase lag case under the low SNR it picks up only the middle network (the one with the highest individual SNR) and generates a large number of false positives.

coupling and low SNR scenario.

6.2.2. Detection of multiple concurrently active networks

In this section we describe the results obtained by simulating three networks whose activity overlapped in time, as illustrated in Fig. 2. To this end we filtered the simulated data in the 8–12 Hz band and calculated the time varying cross-spectral tensor by averaging over trials the outer product of Hilbert transform coefficients of the data at each time slice. We thus obtained matrix $\mathbf{C}^{XX}$, see equation (5), which is ready to be used in PSIICOS analysis pipeline.

Fig. 5 shows the source-space spatial structure of the simulated data scan depicting top 0.1% of connections with the highest value of the source-space connectivity statistic for PSIICOS and three other methods. As one can see only the PSIICOS technique retains reasonable operation for all range of the studied conditions. Consistent with our previous

results the iDICS technique performs nearly as well as PSIICOS in the close to $\pi/2$ mean phase lag case. The MNE GCS technique for the high SNR case quite reliably picks the two frontal networks for both values of the mean phase lag but completely stops operating for the low SNR and near zero mean phase lag case. For the close to $\pi/2$ mean phase lag case under the low SNR it picks up only the middle network (the one with the highest individual SNR) and generates a large number of false positives.

Regressing the time-resolved and vectorized sensor-space cross-spectrum projected away from the SL subspace onto the mean network topographies obtained by averaging within each of the three clusters of edges in Fig. 5 allows recovering the synchrony profiles. Fig. 6 depicts the time windows during which each pair of interacting sources is active. Here, we exploited the vectorized form of the time-resolved cross-spectrum and after debiasing it by removing the spatial leakage component used the simplest possible "source" timeseries estimation procedure. The
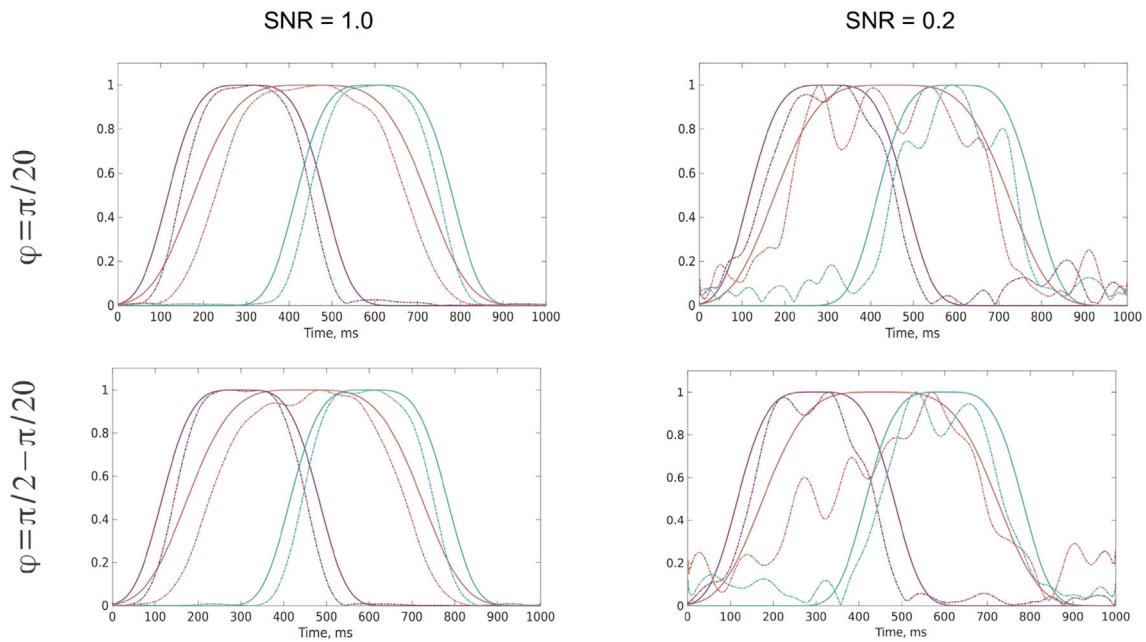
Fig. 6. Temporal profiles of the simulated networks for two phase lag values and for two different SNRs obtained by PSIICOS. Solid lines represent true simulated profiles and dashed lines correspond to the recovered traces.
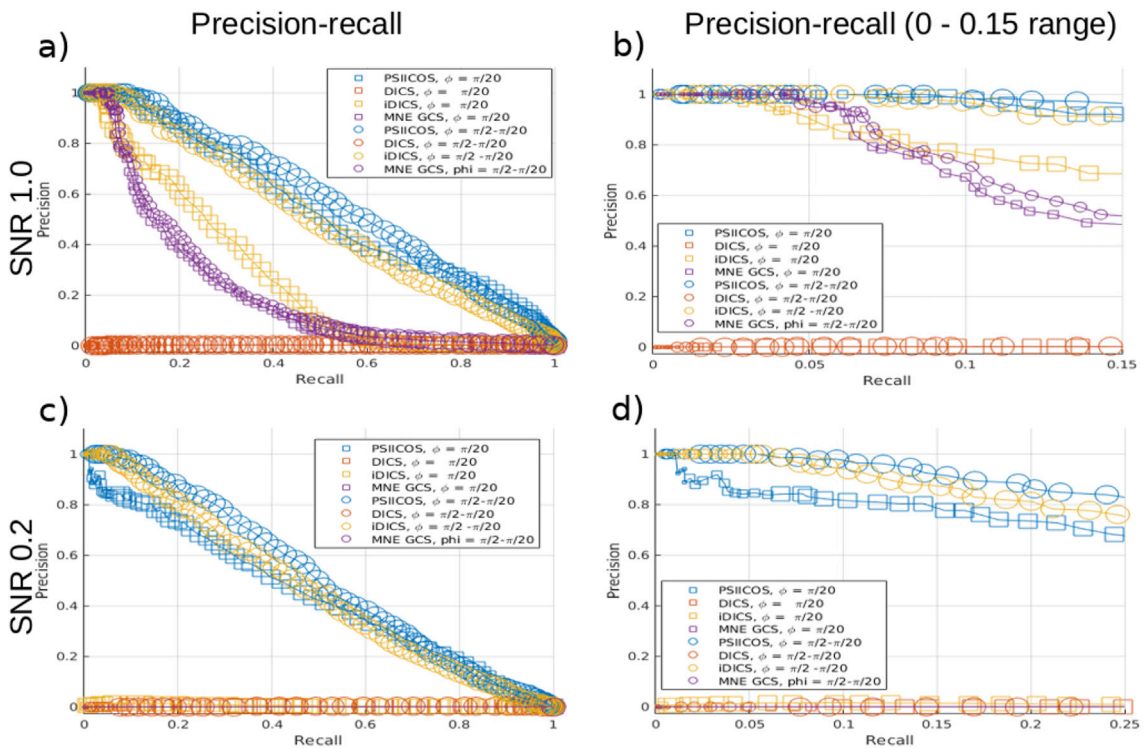

Fig. 7. Comparative analysis of PSIICOS against three other methods in the task of detecting three simultaneously active simulated networks. Panels a, c show the entire precision-recall plot while panels b), d) focus on the 0–0.15 range.

procedure of obtaining these synchrony profiles resembles that used to calculate the time series in the dipole fitting task with the only difference that here we operate in the product space of the coupled source topographies.

Further, to systematically illustrate the comparative analysis of the four techniques considered in this paper, we are showing in Fig. 7 the modified precision-recall plots where as described earlier we encoded with marker size the number of true networks the detected connections come from. The left half of the plots shows the entire precision-recall plot and panels b) and d) focus on the 0–0.15 range. As we can see
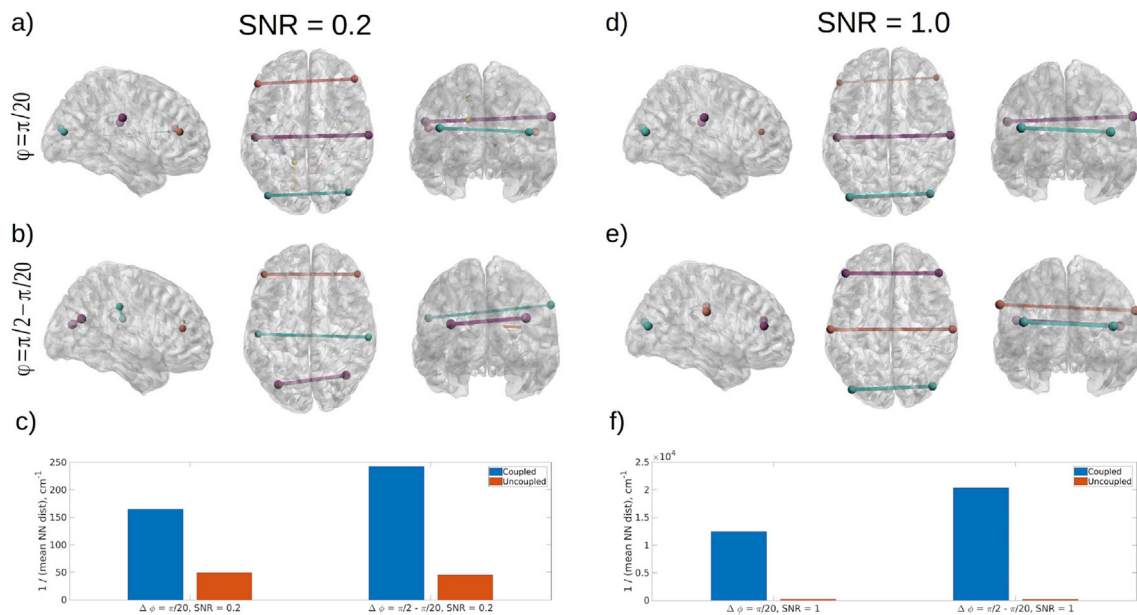
Fig. 8. Bootstrap analysis of PSIICOS results stability for two phase lag values and for two different SNRs.
a), b), d), e) – stable networks – are shown with edges whose ends correspond to the coupled cortical regions. The saturation of the color used to plot the edge and the node is directly proportional to the reproducibility parameter η assessed with the bootstrap procedure. The edges whose nodes appeared to be closer than 1 cm apart are plotted in the same color. Panels c) and f) show reproducibility index η for two mean phase lag values obtained using the described bootstrapping procedure for two different SNR values, SNR = 0.2 and SNR = 1 respectively.
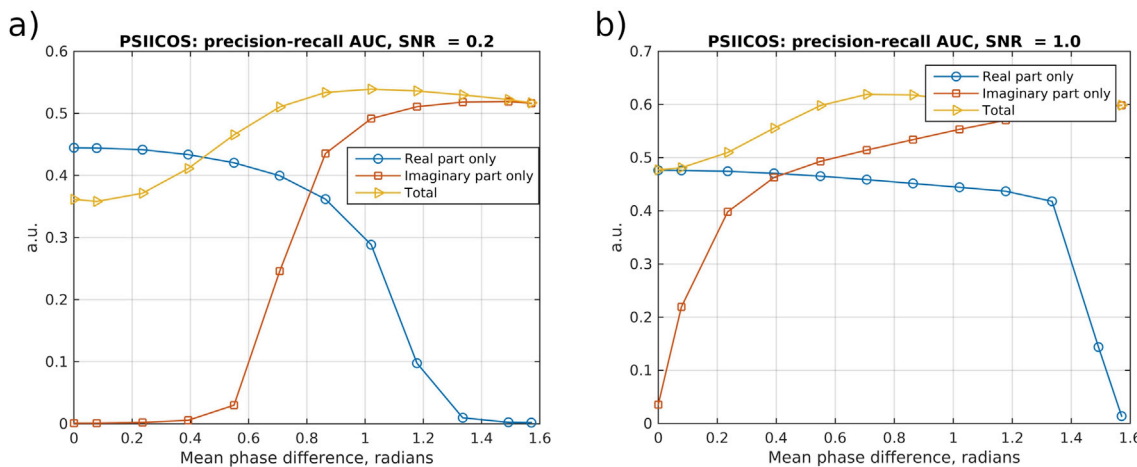

Fig. 9. Performance of PSIICOS as a function of mean phase lag, a) - low SNR and b) - high SNR case. For the close to $\pi/2$ mean phase lag values the information about the interacting sources is primarily contained in the imaginary part of the cross-spectrum. Thus, the use of the imaginary part only (equivalent to iDICS) allows achieving high performance which deteriorates as the mean phase lag gets reduced. On the contrary, for close to zero mean phase lags the coupling information is primarily present in the real part. The real part is contaminated by the SL component that can be removed using the PSIICOS projection. Then, the debiased real part is used for detection of networks with close to zero mean phase lag (blue curves). The simultaneous use of both real and imaginary components allows achieving uniform performance over various mean phase lag values (orange curve).

qualitatively these plots confirm the conclusions based upon the visual analysis of the spatial structure of the detected connections depicted in Fig. 5.

The metrics used so far assessed the performance in a threshold free manner. When applied to real data we suggest to use the bootstrap procedure described in 2 to assess the stability of the observed network patterns. The following figure illustrates the results of the proposed bootstrapping procedure as applied to the realistically simulated data (see Fig. 8).

As demonstrated by our simulations the proposed approach allows achieving superior performance in detecting networks of coupled sources

with both near-zero and close to $\pi/2$ mean phase lags. It turns out that PSIICOS technique provides a uniform detecting performance on the entire range of mean phase lag values. To illustrate this point we applied the proposed technique to the analyses of the simulated 3-networks data for a grid of mean phase-lag values in the 0 to $\pi/2$ range. We did so for two SNR values and compared three different approaches: using the imaginary part only (iDICS), the projected real-part only and the total projected cross-spectral matrix (PSIICOS). Fig. 9 shows the observed performance quantified as precision-recall areas under curve (AUC) vs mean phase lag values. For the close to $\pi/2$ phase lag values the information about the interacting sources is primarily contained in the
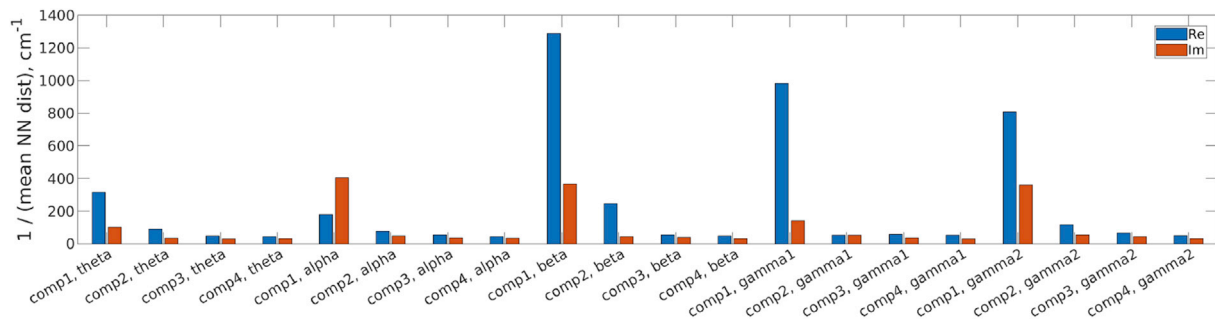
Fig. 10. Bands with most reproducible networks as determined by the bootstrap analysis performed by repeatedly selecting a subset of epochs, computing the cross-spectrum tensor by averaging over these epochs and applying the PSIICOS procedure. The bars correspond to the reproducibility index computed as inverse average distance to the closest neighbour for singular networks found in the real and imaginary parts of the cross-spectrum for the four most prominent singular components (1–4) of the real (blue) and imaginary (yellow) parts of the PSIICOS projected vectorized cross-spectrum.

imaginary part of the cross-spectrum. Indeed, see Fig. 9, the use of the imaginary part only allows achieving high performance for close to $\pi/2$ mean phase lag values. For the realistic $SNR = 0.1$ the performance briskly deteriorates as the mean phase lag angle departs $\pi/2$ neighborhood. On the contrary, for close to zero mean phase lags the coupling information is primarily present in the real part. The real part is contaminated by the SL component that can be efficiently removed by the proposed projection procedure. Then, the projected real part can be used for detection of networks with close to zero mean phase lag, but performance of the SL-debiased real part also deteriorates as the mean phase lag value leaves the realm of nearly zero mean phase lags. The proposed PSIICOS technique allows for the simultaneous use of both SL-debiased real and imaginary components to achieve a uniform performance over various mean phase lag values.

6.3. Application to real data

While the focus of the present study is to outline a novel methodological framework for connectivity estimation and validate it using simulated MEG data, it is important to illustrate how the method behaves with real experimental MEG data. Yet a full group-level analysis using real data and systematic comparisons with other methods on the same dataset would be beyond the scope of this methodological article. We therefore sought to illustrate the application of the PSIICOS technique on sample MEG data and evaluate its robustness. We are aware that real data cannot be used as a benchmark for ground truth as can be done with simulations, but they can illustrate realistic application of the technique and assess the robustness of the method with regards to data variability for instance by resampling the available data using bootstrapping.

Band specific analysis revealed the distribution of reproducibility as shown in Fig. 10 where the inverse mean distance to the nearest neighbour values were plotted in 5 frequency-bin groups for the real and

imaginary part components shown side-by-side. As we can see, networks found using the real part of the cross-spectrum appear to be more reproducible than those obtained from the imaginary part. Most reproducible networks from the real part are found in the theta, beta and both gamma bands. The reproducible networks from the imaginary part of the cross-spectrum belong to alpha, beta and higher gamma bands. It is noteworthy that while real component based networks are in general characterized by higher reproducibility, it is not the case for the alpha band. Figs. 11–13 show the spatial structure of the networks found in these bands with the edges whose ends correspond to the coupled cortical regions. The edges whose nodes appeared to be closer than 1 cm apart were plotted in the same color. Overlapping edges were depicted with larger markers and line-width parameter. Edge transparency was adjusted in accordance with the density of edges in a cluster including the overlaps. Also, for each reproducible component we plot its temporal profile as the right singular vector of the corresponding part of the time-resolved cross-spectrum.

Analysis of the real-part of the cross-spectrum revealed the following networks with dominantly low phase lag coupling. In the theta band, Fig. 11a we see the networks connecting right orbito-frontal region implicated in the sensory integration processes with left bilateral parieto-temporal junction area found to be active during the imagery of movement Hanakawa et al. (2008). Additionally, we see the cross-lateral network linking the two parietal regions. In the beta band we observe mechanistically plausible cross-lateral coupling between the ventral visual pathway and the hand representation zone of the right motor cortex (see Fig. 12a). Additionally, we see the interaction between hand representation areas of the right motor/premotor and the left sensory cortices, Fig. 12b which is partly consistent with the observations reported in Lamm et al. (2007) and related to the fMRI study of mental rotation task as well as with the functional coupling profiles discovered in (Striem-Amit et al. (2017)) for healthy controls. Lastly, we have found
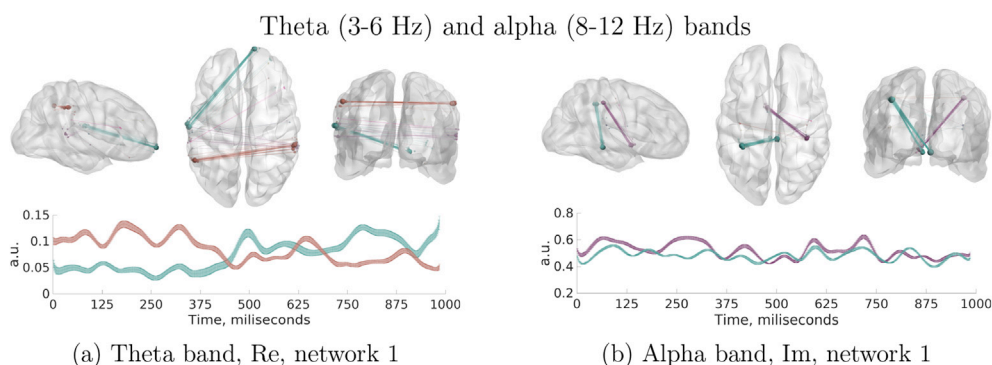

Theta (3-6 Hz) and alpha (8-12 Hz) bands

(a) Theta band, Re, network 1

(b) Alpha band, Im, network 1

Fig. 11. Spatial structure and temporal dynamics of the most reproducible networks found in theta (3–6 Hz) and alpha (8–12 Hz) bands.

Beta band (16-24 Hz)

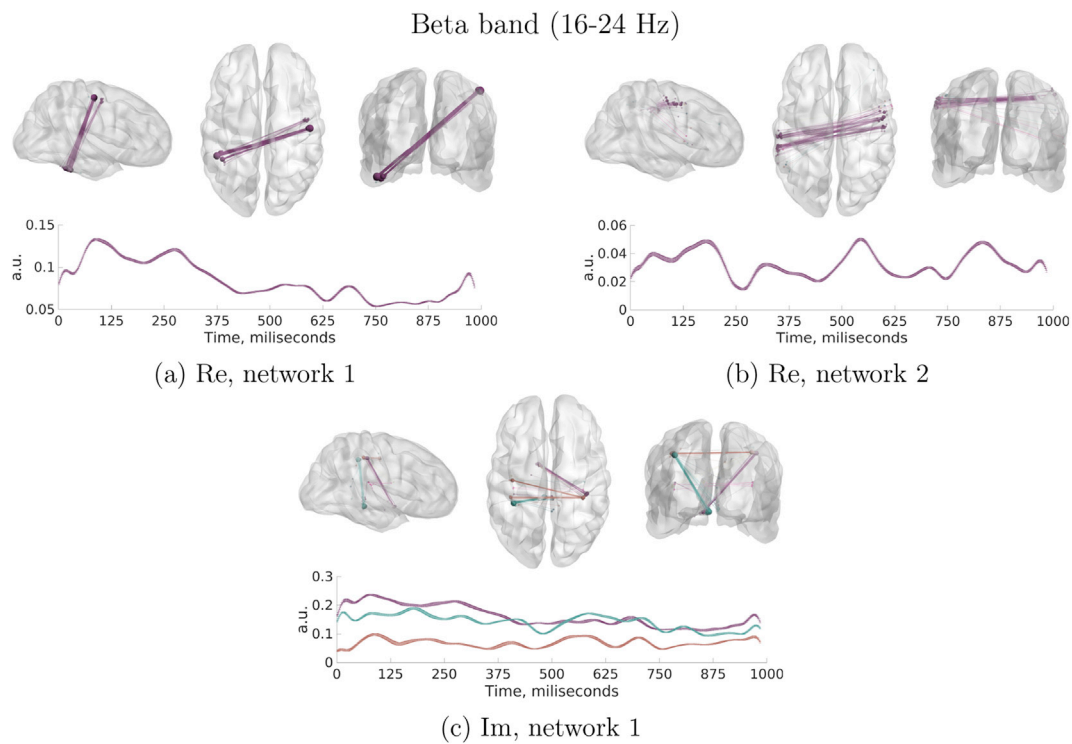(a) Re, network 1

(b) Re, network 2

(c) Im, network 1

Fig. 12. Spatial structure and temporal dynamics of the most reproducible networks found in beta (16–24 Hz) band.

the interaction of the hand area in the right motor cortex with the left temporal pole in the lower gamma range, Fig. 13a, and with left orbito-frontal region in the upper gamma range, Fig. 13b. The plausibility of these findings is supported by the hypothesized role of the left temporal pole which includes " … visual discrimination of two-dimensional pictures, and the mnemonic functions of matching and learning" (Dupont (2002)). Networks seen in the imaginary part of the cross-spectrum include alpha-band coupling of bilateral sensory regions with central inferior structure of the cortex, Fig. 11b as well as the cross-lateral connections between hand related sensory cortices in the beta band, Fig. 12c.

We have also compared the results of our connectivity analysis and

matched them against the specific induced power cortical distribution profiles, see Section 8.5 in the Appendix. As we can see most of the discovered networks, except for one bilateral network in the theta-band, do not have both ends in the areas with dominating power. At the same time, the right sensorimotor site, a node for most of our networks, coincides with dominant activation area. Based on the crucial role of the right sensorimotor cortical area discovered in the original study De Lange et al. (2008) and given that we did not perform a seed based analysis but rather a full-blown all-to all coupling assay, we find these results reassuring.

lower gamma (30-60 Hz) and higher gamma (65-85 Hz) bands

(a) Low gamma band, Re, network 1

(b) Gamma band, Re, network 1
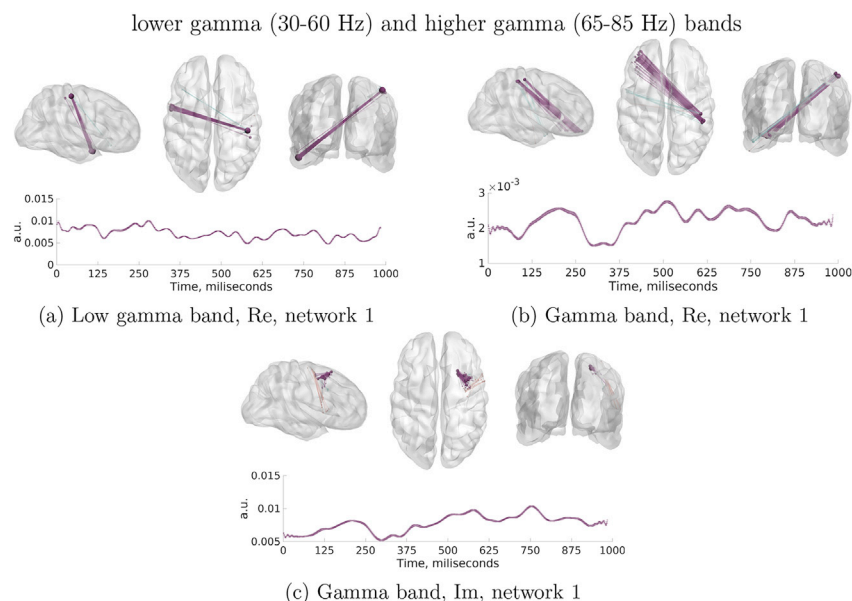
(c) Gamma band, Im, network 1

Fig. 13. Spatial structure and temporal dynamics of the most reproducible networks found in lower gamma (30–60 Hz) and higher gamma (65–85 Hz) bands.

7. Discussion

We have described a novel method for detection of within frequency coupling based on non-invasive MEG and EEG data. The proposed framework demonstrates that it is possible to target the true instantaneous linear coupling with non-invasive recordings. This is achieved by the proposed projection procedure that operates in the space of sensor signals cross-spectral matrices and allows for efficient suppression of the spatial leakage (SL) contribution to the real part of the cross-spectral matrix. It turns out that while the subspace modulated by the real part of the source space cross-spectrum and the subspace that encapsulates the SL power overlap it is quite straightforward to build a spatial projector to banish almost all of the SL power (e.g. 95%, see Fig. 3), and yet remain sensitive to the majority of zero-phase coupled sources. As shown by means of simulations the proposed technique allows gaining sensitivity over the entire range of phase-lag values, see Fig. 9.

Using realistic simulations we have extensively investigated the proposed technique (PSIICOS) and compared its performance against several other methods such as the DICS, the imaginary DICS and the Geometric Correction Scheme (GCS). The PSIICOS technique consistently outperformed the other three methods in both fixed configuration with three concurrently active networks and Monte-Carlo studies under a wide range of realistic noisy conditions and phase-lag values. Importantly, at the same time PSIICOS performs uniformly for the entire range of mean phase lag values.

Numerous techniques for non-invasive detection of functionally coupled networks have emerged recently. Should we have access to the actual signals reflecting the activity of each individual network's node, we could use the coherence function that reflects linear (from the linear time-invariant systems theory point of view) relationship between the signals. However, the activity of cortical generators as measured by the non-invasive sensors is only available in the form of a mixture of activation signals from multiple sources and thus the direct use of sensor signals leads to erroneous results when the spatial leakage effect masks the true functional coupling. To overcome this problem (Nolte et al. (2004a)) suggested the use of the imaginary part of the cross-spectrum as a sensor-space statistics insensitive to the SL effects. This triggered the appearance of a range of methods, e.g. (Stam et al. (2007), Vinck et al. (2011), Ewald et al. (2014)) exploiting the imaginary part of the sensor-space cross-spectrum. While some of them do render an advantage over Nolte's imCoh technique they are all unable to detect zero phase coupled networks as the imaginary part of the sensor-space coherence is not modulated by the real part of the source-space cross-spectrum that carries the information about the actual zero-phase coupling. For zero or close-to-zero mean phase lags SNR of the imaginary part of the sensor-space cross-spectrum is not sufficient to produce a reliable detection, see Fig. 9. At the same time, the use of the raw real part of the sensor-space cross-spectrum is not possible due to the spatial leakage effect. As we have shown here, the use of LCMV beamformer-based inverse operator to unmix the sensor data, as suggested by the DICS technique, does not provide the necessary fidelity and the subsequent use of the resultant source-space coherence fails to deliver the necessary performance under the realistically low SNR.

The approach presented here is most closely related to the geometric correction scheme (GCS) by Wens (Wens et al., 2015), originally introduced in application to the analysis of source-space envelope coupling and compared against the data-driven timeseries orthogonalization techniques (Hipp et al. (2012), Colclough et al. (2015)). The GCS approach suggests the use of a seed-node topography combined with the inverse operator's row corresponding to the probed source location for removing the spatial leakage effect associated with the seed source only. In contrast, instead of using a seed source topography and removing the signal leakage from the single (seed) source, the PSIICOS approach operates in the product space of coupled source topographies and creates the projector that takes into account the SL-contributions from all possible sources. The use of SVD allows building a projector that

efficiently utilizes the degrees of freedom and concentrates the largest amount of the undesired SL power in the subspace of the smallest dimension. This projection operation is applied to the sensor-space cross-spectral matrix debiasing it from the SL-effect. Similarly to GCS, PSIICOS allows us to visualize the dynamics of interaction-dependent cross-spectrum in the sensor space and supports the subsequent sensor-space analysis (not pursued in this paper). For example, given the growing utility of the machine learning approaches in neuroimaging data analyses, the projection operation, forming the foundation of PSIICOS, allows us to obtain the features reflecting true connectivity yet in a relatively compact product space of sensor signals. PSIICOS projection can also be applied to the vectorized single trial outer products of the sensor space data and then utilized for discovery of cortical locations with significant envelope correlations.

As we have demonstrated, the generative equation point of view allows interpreting the task of estimation of the sensor-space cross-spectrum generative model parameters (c_{ij}) as a standard underdetermined linear regression problem, routinely addressed in non-invasive neuroimaging techniques. This approach shows a clear way for introducing much needed priors into the connectivity estimation task. The priors can be extracted by means of diffusion tensor imaging and represented using the probabilistic distribution to be then naturally exploited within the Bayesian paradigm. Less specific and simpler priors, based on sparsity, can also be utilized, and an approach similar to that described in (Strohmeier et al., 2016), exploiting the mixed fractional norms of the obtained solution, can be utilized to build sparse solvers explaining the observed sensor space cross-spectrum with activity of a small number of elementary source-space networks.

Also, following the parametric estimation path, it is possible to apply the extension of dipole fitting techniques including the modified RAP-MUSIC algorithm to the SL-free cross-spectral matrix. In fact, (Ewald et al. (2014)) describes the use of the MUSIC approach for analysis of the imaginary part of the cross-spectrum based on the MUSIC metrics, but as outlined earlier, because of the sole use of the imaginary part of the cross-spectrum, the proposed approach fails to be sensitive to zero phase-lag coupled networks. Also, the computational time of the procedure described in (Ewald et al. (2014)) is high and the authors resort to the two stage procedure to avoid the scan over N^2 source pairs. The vectorized form of the cross-spectrum and the corresponding generative equation can serve as a basis for development of the RAP-MUSIC approach where elementary networks replace the dipoles in the original derivation of this technique (Mosher and Leahy (1999)). RAP-MUSIC suggests recursive projections away from the subspace spanned by the topographies of the sources found so far. When applied to the vectorized cross-spectrum to remove the detected elementary network consisting of nodes A and B such a projection will remove only the contribution from the specific pair and the projected spectrum will retain the other networks formed with node A to other nodes, except for node B and the networks formed with node B to all other possible nodes, but node A. This means that using the RAP-MUSIC approach applied to the vectorized SL-debiased cross-spectrum we should be able to study complex networks consisting of more than one pair of nodes. It is worth investigating whether or not this procedure addresses the issue raised in Mahjoory et al. (2017) when the beamforming estimates and the global MNE solutions resulted into different connectivity patterns.

In the current vectorized implementation in MATLAB, calculation of the projection matrix for the cortical source model with 7000 nodes takes less than one second of computation time and has to be done once per subject, given the sensor positions are fixed or the data are corrected for the movements. Then, our vectorized implementation of the source-space scan over 7000×7000 sites takes half a second time on a modern laptop. Therefore, the proposed approach is computationally efficient and makes the bootstrap analysis for investigation of the observed networks' stability feasible as demonstrated here.

State-of-the-art MEG/EEG source-space interaction metrics that ignore zero-phase coupling, lead to false positives Matias Palva et al. (2018) and true negatives. While the former problem has recently been addressed (e.g. Wang et al. (2018)), a solution for the latter issue has not been proposed so far. In this work, we provide the first demonstration that it is possible to probe true instantaneous linear coupling non-invasively. Given the strong evidence of the existence of such low-latency coupling as seen in the invasive animal studies, we believe, the PSIICOS technique described here will significantly expand the capabilities of the modern functional network analysis tools.

7.1. Strengths and limitations of the PSIICOS framework

The method proposed here provides a novel solution to exploring interactions in MEG data and can selectively address spatial leakage even in the case of zero or close-to-zero phase coupling. This overcomes inherent limitations of methods exploiting the imaginary part of the cross-spectrum or data-driven orthogonalization approaches, which by definition ignore zero-phase interactions (and have weak sensitivity for phase lags in the vicinity of zero). Note however that PSIICOS requires a statistical procedure based on bootstrapping and that it is not entirely immune to false positives in the presence of uncoupled sources with power profiles that are significantly higher than that of the coupled sources.

Our main focus here is the novel projection scheme that allows us to significantly suppress the contributions of spatial leakage to the sensor-space cross-spectrum and obtain a novel generating equation (9) that permits rendering network estimation task as a source estimation problem but in the product space of sensor signals. In order to conduct the required performance checks, we have chosen the simplest possible inversion strategy for this equation. Even with this simple estimation approach our results show potentially superior performance of the proposed technique over a range of other relevant methods and nearly uniform sensitivity to all range of mean phase difference values between the time series of the coupled sources including zero and near-zero phase delays. Capitalizing on the work described in Darvas F (2005) we have also suggested a bootstrap procedure that can be used to test for stability of the observed results.

In case there are true networks present in the data the proposed bootstrapping procedure is not likely to generate a network produced by a pair of active but functionally uncoupled sources as long as the power of these uncoupled sources does not significantly exceed the power in the true networks' nodes. If the data contain multiple not functionally coupled high-power sources, the proposed procedures may lead to false detections. Also, given the described way of focussing on the top values of the ρ scan we are likely to miss some true networks.

The best way to address both of these problems is to develop an efficient statistical test operating on the basis of H_0 distribution. To be useful, this test, however, should attempt to preserve sensor-space power distribution, while destroying zero and close to zero phase coupling. The tests developed so far for assessing linear synchrony are primarily adapted to measures not sensitive to instantaneous coupling. Moreover, applying techniques based on randomization of ICA component time series does not provide a suitable solution when zero or close-to-zero coupling needs to be detected. A better approach based on source space phase randomization that would destroy mutual phases but preserve the smoothness of the phase response of individual activations is needed to address these issues. However, since the algorithms for surrogate data generation match their properties against those of the original data in the sensor space Haufe and Evald (2016), it may be difficult for such techniques to distinguish between instantaneous correlation caused solely by volume conduction and the true zero-phase coupling. Therefore more consolidated efforts are needed to supply a robust statistical testing framework tailored to connectivity analysis techniques such as the one described here.

Despite these limitations, PSIICOS represents a first attempt at detecting zero and close-to-zero phase lag interactions from MEG data. To the best of our knowledge, it is also for the first time that MEG/EEG based linear coupling estimation task is rendered as a multidimensional regression problem, similar to that encountered in the classical inverse modeling of this data. This opens up a rich pool of exciting opportunities to adapt the plethora of regularization based or parametric techniques developed in the field to tackle the functional coupling estimation problem.

Acknowledgment

Appendix

PSIICOS projection: accommodation of arbitrary orientation

Anatomically, the dipole orientations coincide with the direction of apical dendrites of the pyramidal neurons and therefore appear to be predominantly orthogonal to the cortical mantle. Modern tools of MRI data analysis allow for a very accurate extraction and precise parametrization of the cortical surface with number of nodes on the order of tens of thousands, which in turn results into reasonable accuracy of orientation specification. The uncertainty that remains may be efficiently modeled with such techniques as in Lin et al. (2006).

Because of memory and processing time limitations when performing exploratory source-space synchrony analysis we have to use a significantly downsampled version of the cortex that contains only several thousands of nodes. Such downsampling drastically reduces the requirements to computational resources but introduces significant uncertainty in orientations of elementary sources.

Therefore, it became a common practice to restrict the source space to the downsampled cortical mantle and to model the arbitrary orientations of node dipoles by representing each elementary source with the triplet of orthogonal dipoles. In case of MEG, since the magnetic field outside the spherical conductor produced by a dipole with radial orientation is zero, the triplet can be efficiently replaced by a pair of dipoles in the tangential plane, calculated for each node.

For an arbitrary orientation vector at some i-th vertex $\theta_i = [\theta_i^x \theta_i^y]^T$ the corresponding dipole topography is $\mathbf{g}_i^{\theta_i} = [\mathbf{g}_i^x \quad \mathbf{g}_i^y]\theta_i$, where $\mathbf{g}_i^x$, $\mathbf{g}_i^y$ are the topographies of the two orthogonally oriented dipoles in the tangential plane at the i-th vertex. Varying the orientation angle we will obtain an infinite set of SL topography vectors $\mathbf{q}_{ii}^\theta = vec(\mathbf{g}_i^{\theta_i}\mathbf{g}_i^{\theta_i T})$. It is easy to show that in case of two-dimensional tangent space (as we have in MEG) all these vectors

belong to the three-dimensional subspace $S_{\theta_i} = span(\mathbf{q}_{ii}^{xx}, \mathbf{q}_{ii}^{yy}, \mathbf{q}_{ii}^{xy} + \mathbf{q}_{ii}^{yx})$.

Therefore, in order to accommodate the arbitrary orientation constraint, equation (7) has to be replaced by

$$\mathbf{F} = \left[\mathbf{q}_{11}^{xx}, \mathbf{q}_{11}^{yy}, \mathbf{q}_{11}^{xy} + \mathbf{q}_{11}^{yx}, \ldots, \mathbf{q}_{LL}^{xx}, \mathbf{q}_{LL}^{yy}, \mathbf{q}_{LL}^{xy} + \mathbf{q}_{LL}^{yx} \right] \tag{11}$$

The projection matrix is then found as described in Step 3 in section 2.3.

PSIICOS projection: impact of the rank parameter

We have studied the dependence of the attenuation factors in all three subspaces as a function of the projection rank. Fig. 14 shows the average attenuation of the power in the three subspaces as a function of the projection rank. To obtain this plot we performed a Monte-Carlo analysis. At each iteration we randomly selected a subset of 200 sources and calculated all the vectors from the three subspaces $S^{SL}, S^{\Re}, S^{\Im}$. We used sources with fixed orientations orthogonal to the cortical mantle. We then varied the rank of the projection and computed the projected versions of these elementary network topography vectors. To quantify the attenuation effect, we calculated the average ratio of the original to the projected vector norms for each value of the projection rank. We repeated this process 100 times and averaged the result.

Because of the intersection of the S^{SL} and $S^{\Re}$ subspaces the projection operation attempting to suppress the SL component power inevitably leads to suppression of power in the $S^{\Re}$ subspace. The less power in the $S^{\Re}$ subspace is suppressed for the fixed SL power suppression factor the better the performance is. Therefore, in addition to the attenuation curves for the subspaces we have also plotted the log-ratio of attenuation coefficients observed for the vectors in the $S^{\Re}$ subspace to that for the S^{SL} subspace. The use of the SVD factorization to form the projection operator allowed for the observed significantly faster reduction in the spatial leakage subspace S^{SL} power than in the $S^{\Re}$ subspace. In other words, we see that the increased projection rank leads to a greater dominance of power in $S^{\Re}$ subspace over that in the S^{SL} subspace.

We have thus shown that cross-spectrum $\mathbf{C}^{\perp}(t.f_0)$ projected away from the SL subspace is dominated by the energy in the true connectivity subspace. The product-space topographies of the interacting pairs can be easily computed as $\overline{\mathbf{q}}_{ij} = \mathbf{P}\mathbf{q}_{ij}$ and the corresponding generative model of the projected cross-spectrum (see equation (9)) can be used to perform inference on the source-space cross-spectral coefficients $c_{ij}^{ss}(t.f_0)$.
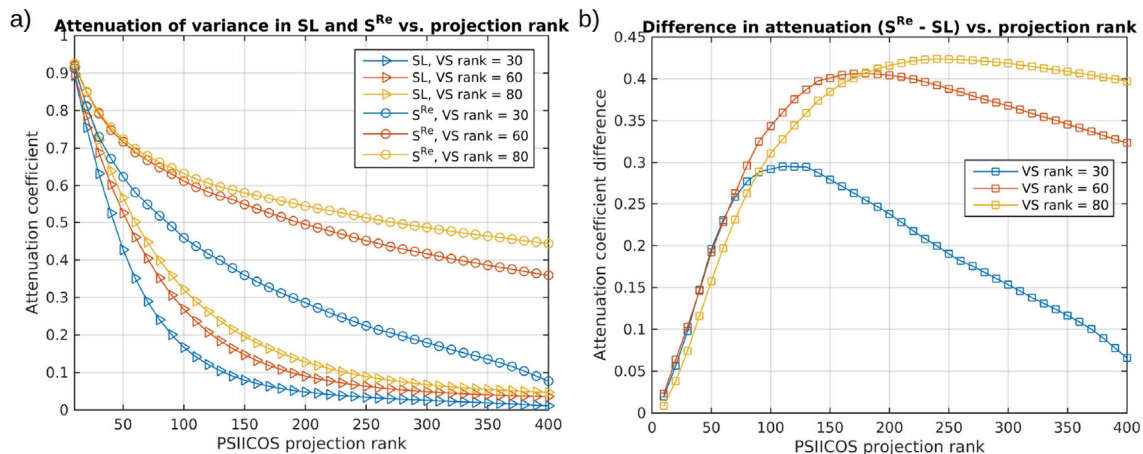

Fig. 14. a) Attenuation of variance in SL and $S^{\Re}$ subspaces as a function of projection rank for three different virtual sensor (VS) space dimensions. b) Difference in attenuation factor for $S^{\Re}$ and SL subspaces as a function of projection rank for three different virtual sensor (VS) space dimensions. These curves allow making an informed decision regarding the choice of the projection rank. We suggest choosing PSIICOS projection rank value corresponding to the largest differential attenuation.

PSIICOS projection: forward model inaccuracy effect

The described projection procedure requires forward model (FM) operator that in a realistic setting inevitably comes with inaccuracies. In this section we study the performance of the proposed projection operation in presence of the structured and non-structured errors in the forward model.

We used two models of noise in this study. The first model corresponded to spatially unstructured noise and was implemented simply by adding the appropriately scaled random noise to the FM model operator matrix. We sampled form the $N(0,1)$ distribution to generate a FM noise realization matrix. We then scaled this by multiplying its elements by the square-root of the mean trace value of matrix $\mathbf{G}\mathbf{G}^T$ where $\mathbf{G}$ is the forward model matrix. We then added this matrix to the actual (true) forward model and adjusted the amount of noise by parameter α.

The second model corresponds to a more realistic scenario of spatially structured distortion. To generate the spatially structured noise matrix we used the head models computed for $N = 10$ subjects and calculated the pairwise differences between the forward models for each pair of subjects. We then computed the structured noise matrix as the average of these pair-wise differences. We then standardized the resulting structured noise matrix added it to the true forward model. As in the previous case we adjusted the amount of noise by parameter α used to scale the noise matrix.

Potentially, the inaccuracies in the FM may cause the simultaneous reduction in the SL power attenuation and the decrease of $S^{\Re}$ subspace power. We performed Monte-Carlo simulations to numerically study these effects. At each iteration we randomly selected a subset of 200 sources and calculated mean attenuation ratio for the three subspaces. We did so for both structured and unstructured noise cases and for two different projection rank values (350 and 500). The results are shown in Fig. 15.

We can see that while the inaccuracies in the forward model do cause deterioration of performance of the proposed projection scheme, for typical

MEG FM noise levels of 10% (Mosher et al. (1999)) we have almost the same value of the SL power attenuation and only about 20% of additional decrease in the $S^{\Re}$ subspace variance.
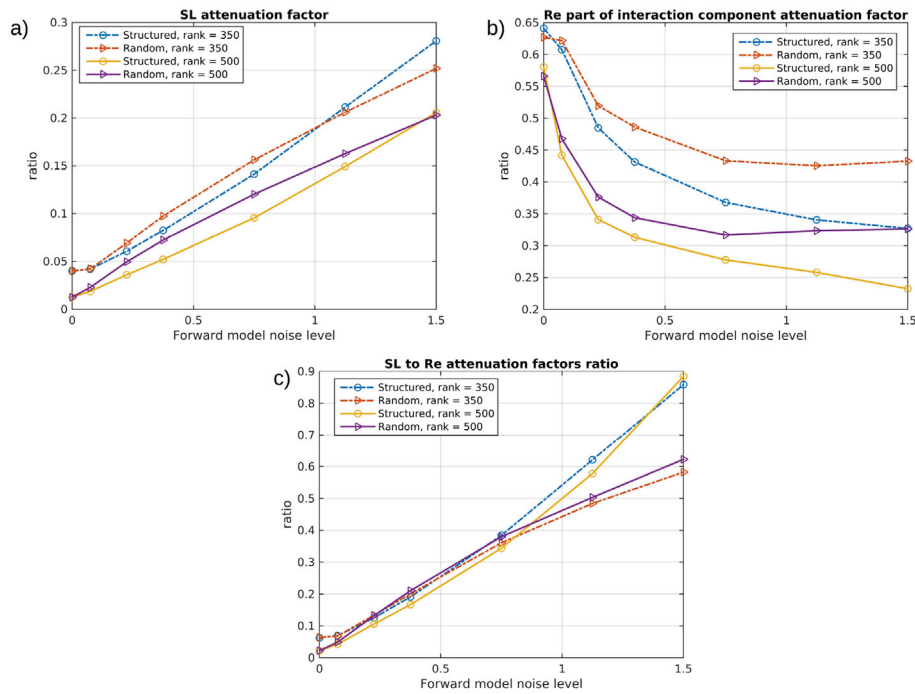

Fig. 15. Effects of FM noise on the projection performance. Panel a) shows the dependence of SL attenuation factor as a function of the FM noise intensity α. From the graph in panel b) we can see the attenuation factor for the variance in the $S^{\Re}$ subspace. As follows from panel c) the extent of suppression of power in the SL subspace as compared to the power in $S^{\Re}$ monotonically decreases with the forward model noise intensity.

Because of the intersection of the S^{SL} and $S^{\Re}$ subspaces attempting to suppress the SL component the algorithm also suppresses the power in the true real interaction subspace $S^{\Re}$. The inaccuracies in the FM increase the undesired suppression of power in the $S^{\Re}$ subspace and decrease the SL power suppression efficiency. Such performance deterioration with the increase of FM inaccuracies intensity can be characterized by the ratio of the attenuation factors experienced by the vectors in the SL and $S^{\Re}$ subspaces. When this ratio is less than one, we can say that the SL power gets decreased more than the power in the $S^{\Re}$ subspace, and therefore, the smaller this ratio the better is the performance of the proposed scheme. We therefore calculated the ratio of the power attenuation factor for the SL subspace to that of the $S^{\Re}$ subspace and plotted it in panel c) of Fig. 15. As we see, the value of this ratio changes smoothly with the growing intensity of the FM noise and remains low for the 10% noise level.

In this section, we have described our numerical studies investigating the deterioration of the performance of the posed projection scheme due to the forward model inaccuracies. Based on the presented numerical results, we conclude that the method is sufficiently robust to tolerate typical FM modeling inaccuracies and can be used in a realistic setting. However, as with many other model-based techniques (e.g. beamforming) the efforts of creating more accurate forward models will have a tangible payoff and therefore need not be neglected.

Performance metrics

Here we detail the Precision-Recall metrics that we used along with more standard ROC curve for comparing the performance of several networks detection approaches. Precision (or positive predictive value), recall (sensitivity) and specificity are defined as follows

$$
\begin{aligned}
precision &= \frac{TP}{TP + FP}, \\
recall &= \frac{TP}{TP + FN} \\
specificity &= \frac{TN}{FP + TN},
\end{aligned}
\tag{12}
$$

where TP, FN, FP, and TN stand for true positives, false negative, false positive, and true negative detections correspondingly. In order to calculate these quantities, we need to label all possible connections between the source-grid nodes as those that belong and those that don't to the simulated networks. Since for simulating the data we used a high-resolution cortical mesh with 15000 grid nodes and for detection step we used a 10 times sparser version of the cortical mesh, we employed the notion of δ-cylinder. Each n-th true network is defined in our simulations by a pair of nodes with coordinates $\mathbf{r}_1^n$ and $\mathbf{r}_2^n$. For each such node we define a set of indices of cortical mesh nodes Ω_1^n and Ω_2^n whose coordinates fall into the δ neighborhood of $\mathbf{r}^{n_1}$ and $\mathbf{r}^{n_2}$, i.e. $\Omega_k^n = \{i\} : (\mathbf{r}_k^n - \mathbf{r}_i) < \delta$ for $k = 1, 2$. A connection between a pair of nodes from Ω_1^n and Ω_2^n subsets (but not within one subset) is considered to be a true connection corresponding to network n.

As we can see, from the last line of equation (12), since all node-pairs that fall within Ω_1^n and Ω_2^n subsets constitute a small fraction of all possible connections and TN is extremely large only high *specificity* values are of interest. Since the ROC curve shows *sensitity vs 1-specificity* we will be primarily

interested in the behavior of this curve for low abscissa values. In our plots, we considered ROC curves in $[0, 0.01]$ false alarm range. At the same time, the precision metrics operates only within the subsets Ω_1^n and Ω_2^n which makes the precision-recall plots a convenient performance metric in our scenario.

Precision-recall (P-R) curve clearly reflects the performance in a single network case. For multiple true networks (which is the case in the second set of simulations) the high area under the P-R curve may be obtained even if only one out of several true networks is detected. In order for the P-R plot to adequately reflect the detection performance in the multiple networks scenario, we encoded with marker size the number of true networks the detected connections come from.

Induced activity power distribution

In order to validate our findings and make sure the obtained networks do not entirely coincide with cortical regions with dominating activity, we are presenting here the band-specific distribution of the induced activity, see Figs. 16–18. These maps were produced using MNE-python software according to the following procedure.

First, in order to compensate for the differences in trials' duration due to varying response latencies we cropped each trial in [-0.5, 1.024] seconds interval which corresponded to the time range of the shortest trial. Then, in order to alleviate the filtering boundary effects, we computed the time-inverted version of each trial and padded the original trial with its time-inverse from left and right. These triple-length trials were then filtered in five frequency bins of interest with the FIR zero-phase filter and cropped back to the [0,1] seconds time interval with 0 corresponding to the stimulus onset of the original, noninverted trial. Next, for the source space with 8194 vertices we computed the MNE inverse operator with loose orientation constraint (loose orientation coefficient = 0.2) and depth weighing (coefficient = 0.6) and applied it to the individual trials. Finally, we averaged squares of the source-level trials both across time and trials and plotted the results.
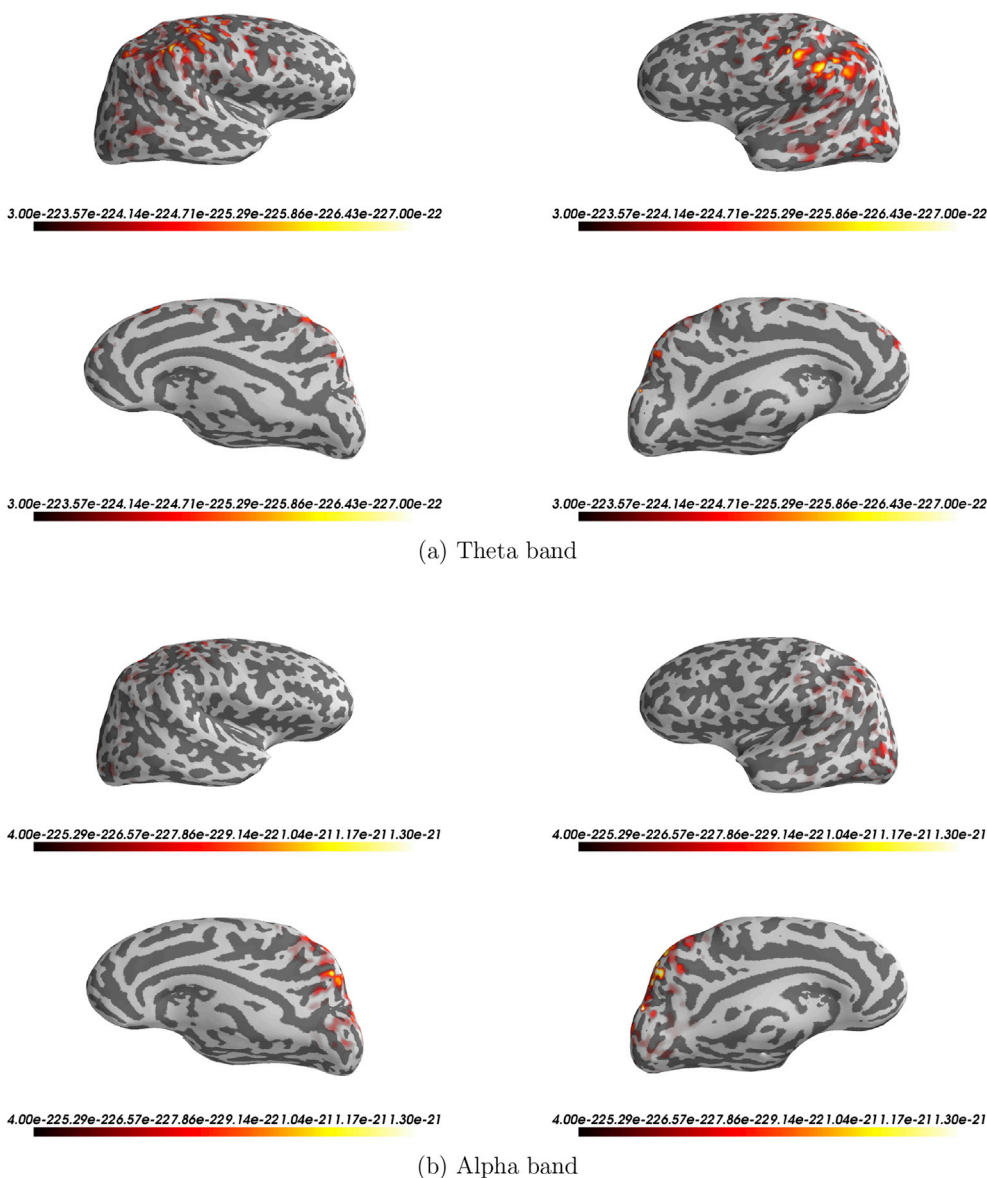

(a) Theta band

(b) Alpha band

Fig. 16. Distribution of induced oscillatory power for theta (3–6 Hz), alpha (8–12 Hz), beta bands.

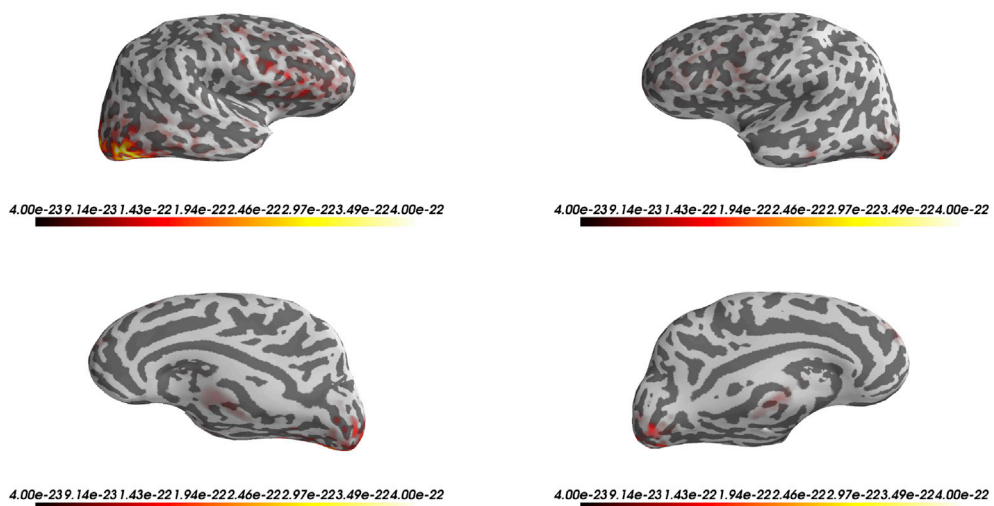6.00e-22 7.29e-22 8.57e-22 9.86e-22 1.11e-21 1.24e-21 1.37e-21 1.50e-21   6.00e-22 7.29e-22 8.57e-22 9.86e-22 1.11e-21 1.24e-21 1.37e-21 1.50e-21

6.00e-22 7.29e-22 8.57e-22 9.86e-22 1.11e-21 1.24e-21 1.37e-21 1.50e-21   6.00e-22 7.29e-22 8.57e-22 9.86e-22 1.11e-21 1.24e-21 1.37e-21 1.50e-21
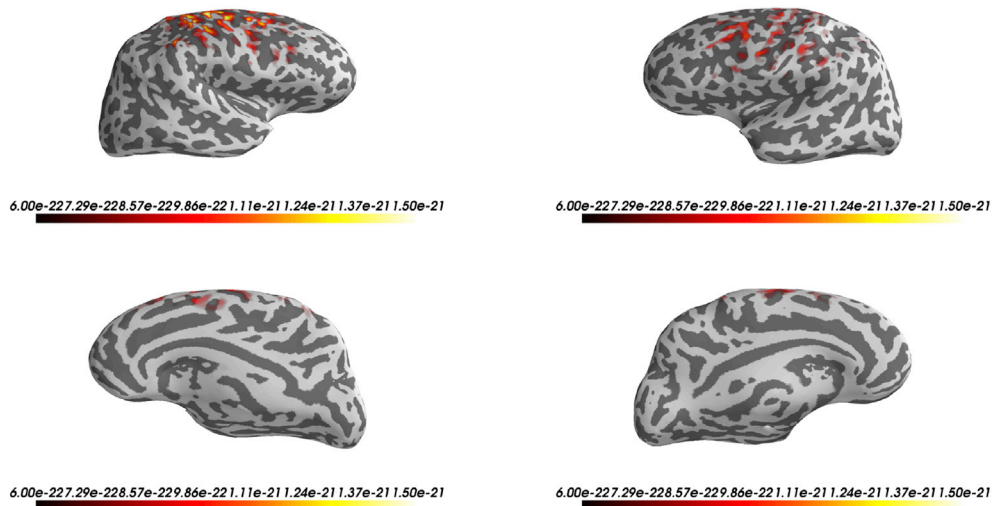
Fig. 17. Distribution of induced oscillatory power for beta (16–24 Hz) band.

1.00e-22 1.71e-22 2.43e-22 3.14e-22 3.86e-22 4.57e-22 5.29e-22 6.00e-22   1.00e-22 1.71e-22 2.43e-22 3.14e-22 3.86e-22 4.57e-22 5.29e-22 6.00e-22

1.00e-22 1.71e-22 2.43e-22 3.14e-22 3.86e-22 4.57e-22 5.29e-22 6.00e-22   1.00e-22 1.71e-22 2.43e-22 3.14e-22 3.86e-22 4.57e-22 5.29e-22 6.00e-22

(a) Lower gamma band

4.00e-23 9.14e-23 1.43e-22 1.94e-22 2.46e-22 2.97e-22 3.49e-22 4.00e-22   4.00e-23 9.14e-23 1.43e-22 1.94e-22 2.46e-22 2.97e-22 3.49e-22 4.00e-22

4.00e-23 9.14e-23 1.43e-22 1.94e-22 2.46e-22 2.97e-22 3.49e-22 4.00e-22   4.00e-23 9.14e-23 1.43e-22 1.94e-22 2.46e-22 2.97e-22 3.49e-22 4.00e-22

(b) Gamma band

Fig. 18. Distribution of induced oscillatory power for lower gamma (30–60 Hz) and gamma (65–85 Hz) bands.

References

Baccalá, A.Luiz, Sameshima, Koichi, 2001. Partial directed coherence: a new concept in neural structure determination. Biol. Cybern. 84 (6), 463–474. https://doi.org/10.1007/PL00007990. ISSN 0340–1200. http://link.springer.com/10.1007/PL00007990.

Baillet, S., Mosher, J.C., Leahy, R.M., November 2001. Electromagnetic brain mapping. IEEE Signal Process. Mag. 18 (1), 14–30. http://ieeexplore.ieee.org/xpl/login.jsp?tp=&arnumber=962275&url=http%3A%2F%2Fieeexplore.ieee.org%2Fxpls%2Fabs_all.jsp%3Farnumber%3D962275.

Baker, Adam P., Brookes, Matthew J., Rezek, Iead A., Smith, Stephen M., Behrens, Timothy, Probert Smith, Penny J., Woolrich, Mark, 2014. Fast transient networks in spontaneous human brain activity. eLIFE 3. http://elifesciences.org/content/elife/3/e01867.full.pdf.

Bastin, Julien, Deman, Pierre, Olivier, David, Gueguen, Maëlle, Benis, Damien, Minotti, Lorella, Hoffman, Dominique, Combrisson, Etienne, Jan, Kujala, Perrone-bertolotti, Marcela, Kahane, Philippe, Lachaux, Jean-philippe, Jerbi, Karim, 2017. Direct recordings from human anterior insula reveal its leading role within the error-monitoring network. Cerebral Cortex (February), 1545–1557. https://doi.org/10.1093/cercor/bhv352.

Bastos, André M., Schoffelen, Jan-mathijs, 2016. A tutorial review of functional connectivity analysis methods and their interpretational Pitfalls, 9 (January), 1–23. https://doi.org/10.3389/fnsys.2015.00175.

Brookes, Matthew J., Woolrich, Mark, Henry, Luckhoo, Price, Darren, Hale, Joanne R., Stephenson, Mary C., Barnes, Gareth R., Smith, Stephen M., Morris, Peter G., 2011. Investigating the electrophysiological basis of resting state networks using magnetoencephalography. Proc. Natl. Acad. Sci. (16) https://doi.org/10.1073/pnas.1112685108.

Brookes, M.J., Woolrich, M.W., Barnes, G.R., 2012. NeuroImage Measuring functional connectivity in MEG : a multivariate approach insensitive to linear source leakage. Neuroimage 63 (2), 910–920. https://doi.org/10.1016/j.neuroimage.2012.03.048. ISSN 1053–8119. https://doi.org/10.1016/j.neuroimage.2012.03.048.

Buzsaki, G., 2006. Rhythms of the Brain. Oxford Univ. Press, New York.

Caetano, Gina, Jousmäki, Veikko, Hari, Riitta, 2007. Actor's and observer's primary motor cortices stabilize similarly after seen or heard motor actions. Proc. Natl. Acad. Sci. Unit. States Am. 104 (21), 9058–9062. https://doi.org/10.1073/pnas.0702453104. ISSN 0027–8424. http://www.pnas.org/content/104/21/9058.

Casanova, M.F., El-Baz, A., Suri, J.S., 2017. Autism Imaging and Devices. CRC Press, Boca Raton London New York.

Chella, F., Marzetti, L., Pizzella, V., Zappasodi, F., Nolte, G., 2015. Third order spectral analysis robust to mixing artifacts for mapping cross-frequency interactions in EEG/MEG. NeuroImage 146–161. https://doi.org/10.1016/j.neuroimage.2013.12.064.Third.

Chella, Federico, Pizzella, Vittorio, Zappasodi, Filippo, Guido, Nolte, Marzetti, Laura, 2016. Bispectral pairwise interacting source analysis for identifying systems of cross-frequency interacting brain sources from electroencephalographic or magnetoencephalographic signals. Phys. Rev. E 1–17. https://doi.org/10.1103/PhysRevE.93.052420.

Colclough, G.L., Brookes, M.J., Smith, S.M., Woolrich, M.W., 2015. NeuroImage A symmetric multivariate leakage correction for MEG connectomes. Neuroimage 117, 439–448. https://doi.org/10.1016/j.neuroimage.2015.03.071. ISSN 1053–8119. https://doi.org/10.1016/j.neuroimage.2015.03.071.

Colclough, G.L., Woolrich, M.W., Tewarie, P.K., Brookes, M.J., Quinn, A.J., Smith, S.M., 2016. NeuroImage How reliable are MEG resting-state connectivity metrics ? NeuroImage 138, 284–293. ISSN 1053–8119. https://doi.org/10.1016/j.neuroimage.2016.05.070.

Darvas, F., Rautiainen, M., Pantazis, D., Baillet, S., Benali, H., Mosher, J.C., Garnero, L., Leahy, R.M., 2005. Investigations of dipole localization accuracy in MEG using the bootstrap. NeuroImage 25 (2), 355–368. ISSN: 1053-8119. https://doi.org/10.1016/j.neuroimage.2004.09.045.

De Lange, F.P., Jensen, O., Bauer, M., Toni, I., 2008. Interactions between posterior gamma and frontal alpha/beta oscillations during imagined actions. Front. Hum. Neurosci. 2 (7) https://doi.org/10.3389/neuro.09.007.2008. ISSN 1053–8119.

Dupont, S., 2002. Investigating temporal pole function by functional imaging. Epileptic Disord. 2002 (9), S17–S22, 2002.

Engel, A.K., Fries, P., Singer, W., 2001. Dynamic predictions: oscillations and synchrony in top-down processing. Nat. Rev. Neurosci. (2), 704–716, 2001.

Ewald, Arne, Avarvand, Forooz Shahbazi, Guido, Nolte, 2014. Wedge music: a novel approach to examine experimental differences of brain source connectivity patterns from eeg/meg data. Neuroimage 101, 610–624. http://www.ncbi.nlm.nih.gov/pubmed/25038442.

Foster, B.L., He, B.J., Honey, C.J., Jerbi, K., Maier, A., Saalmann, Y.B., 2016. Spontaneous neural dynamics and multi-scale network organization. Front. Syst. Neurosci. 10 (7).

Fries, Pascal, 2015. Rhythms for Cognition : Communication through Coherence, 88(1). https://doi.org/10.1016/j.neuron.2015.09.034.Rhythms.

Greenblatt, R.E., Pflieger, M.E., Ossadtchi, A.E., 2012. Basic mathematical and electromagnetic concepts of the biomagnetic inverse problem. J. Neurosci. Meth. 1–16.

Gross, J., Kujala, J., Hämäläinen, M., Timmermann, L., Schnitzler, A., Salmelin, R., 2001. Dynamic imaging of coherent sources: studying neural interactions in the human brain. Proc. Natl. Acad. Sci. Unit. States Am. 98 (2), 694–699. https://doi.org/10.1073/pnas.98.2.694. ISSN 0027–8424. http://www.pnas.org/content/98/2/694.

Gross, Joachim, Baillet, Sylvain, Barnes, Gareth R., Henson, Richard N., Hillebrand, Arjan, Jensen, Ole, Jerbi, Karim, Litvak, Vladimir, Maess, Burkhard, Oostenveld, Robert, Parkkonen, Lauri, Taylor, Jason R., Van Wassenhove, Virginie, Wibral, Michael,

Schoffelen, Jan-mathijs, 2013. NeuroImage Good practice for conducting and reporting MEG research. Neuroimage 65, 349–363. https://doi.org/10.1016/j.neuroimage.2012.10.001. ISSN 1053–8119. https://doi.org/10.1016/j.neuroimage.2012.10.001.

Hamalainen, Matti, Hari, Riitta, Ilmoniemi, Risto J., Knuutila, Jukka, Lounasmaa, Olli V., 1993. Magnetoencephalography – theory, instrumentation, and applications to noninvasive studies of the working human brain. Rev. Mod. Phys. 65 (2), 413–497. http://journals.aps.org/rmp/abstract/10.1103/RevModPhys.65.413.

Hanakawa, Takashi, Dimyan, Michael A., Hallett, Mark, 2008. Motor planning, imagery, and execution in the distributed motor network: a time-course study with functional mri. Cerebr. Cortex 18 (12), 2775–2788. https://doi.org/10.1093/cercor/bhn036.

Haufe, S., Evald, A., 2016. A simulation framework for benchmarking EEG-based brain connectivity estimation methodologies. Brain Topogr. ISSN 1573–6792 https://doi.org/10.1007/s10548-016-0498.

Hillebrand, Arjan, Stam, Cornelis J., 2014. Recent developments in MEG network analysis. Magnetoencephalography. From Signals to Dynamic Cortical Networks 263–277. http://link.springer.com/chapter/10.1007%2F978-3-642-33045-2_12.

Hillebrand, Arjan, Barnes, Gareth R., Bosboom, Johannes L., Berendse, Henk W., Cornelis, J Stam, 2012. NeuroImage Frequency-dependent functional connectivity within resting-state networks : an atlas-based MEG beamformer solution. NeuroImage 59 (4), 3909–3921. ISSN 1053–8119. https://doi.org/10.1016/j.neuroimage.2011.11.005.

Hipp, Joerg F., Hawellek, David J., Corbetta, Maurizio, Siegel, Markus, Engel, Andreas K., 2012. Large-scale cortical correlation structure of spontaneous oscillatory activity. Nat. Neurosci. 15 (6), 884–890. https://doi.org/10.1038/nn.3101. ISSN 1097–6256.

Hincapie, A.S., Kujala, J., Mattout, J., Daligault, S., Delpuech, C., Domingo, M., Cosmelli, D., Jerbi, K., 2016. MEG connectivity and power detections with minimum norm estimates require different regularization parameters. Comput. Intell. Neurosci. 2016 (March) https://doi.org/10.1155/2016/3979547, 2016(March) ISSN 16875273.

Hincapie, A.S., Kujala, J., Mattout, J., Pascarella, A., Daligault, S., Delpuech, C., Mery, D., Cosmelli, D., Jerbi, K., 2017. The impact of meg source reconstruction method on source-space connectivity estimation: a comparison between minimum-norm solution and beamforming. Neuroimage 156 (7). ISSN 29–42.

Ioannides, A.A., Liu, L.C., Kwapien, J., Drozdz, S., Streit, M., 2000. Coupling of regional activations in a human brain during an object and face affect recognition task, 92, 77–92.

Jerbi, Karim, Lachaux, Jean-philippe, Diaye, Karim N., Pantazis, Dimitrios, Leahy, Richard M., Garnero, Line, Baillet, Sylvain, 2007. Coherent neural representation of hand speed in humans revealed by MEG imaging. Proc. Natl. Acad. Sci. 104 (18).

Kaminski, Maciej, Blinowska, Katrzyna J., 2014. Directed transfer function is not influenced by volume conduction - inexpedient pre-processing should be avoided. Front. Comput. Neurosci. 8 (61). http://www.ncbi.nlm.nih.gov/pmc/articles/PMC4050361/.

Lachaux, J.-P., Rodriguez, E., Martinerie, J., Varela, F.J., 1999. Measuring phase synchrony in brain signals. Hum. Brain Mapp. 8 (4), 194–208. http://www.scopus.com/inward/record.url?eid=2-s2.0-0032757697&partnerID=40&md5=c404423056859241c3cb46401cafabb9. cited By (since 1996)852.

Lamm, Claus, Windischberger, Christian, Moser, Ewald, Bauer, Herbert, 2007. The functional role of dorso-lateral premotor cortex during mental rotation: an event-related fmri study separating cognitive processing steps using a novel task paradigm. Neuroimage 36 (4), 1374–1386. ISSN 1053–8119. https://doi.org/10.1016/j.neuroimage.2007.04.012. http://www.sciencedirect.com/science/article/pii/S1053811907003205.

Lee, B., Park, K.S., Kang, D.-H., Kang, K.W., Kim, Y.Y., Kwon, J.S., 2007. Generators of the gamma-band activities in response to rare and novel stimuli during the auditory oddball paradigm. Neurosci. Lett. 413 (3).

Lin, Fa Hsuan, Belliveau, John W., Dale, Anders M., Hamalainen, Matti S., 2006. Distributed current estimates using cortical orientation constraints. Hum. Brain Mapp. 27 (1), 1–13. https://doi.org/10.1002/hbm.20155. ISSN 10659471.

Luo, Liqun, Rodriguez, Eugenio, Jerbi, Karim, Lachaux, Jean-Philippe, Martinerie, Jacques, Corbetta, Maurizio, Shulman, Gordon L., Piomelli, Daniele, Turrigiano, Gina G., Nelson, Sacha B., Joels, Marian, de Kloet, E. Ronald, Holsboer, Florian, Amodio, David M., Frith, Chris D., Block, Michelle L., Zecca, Luigi, Hong, Jau-Shyong, Dantzer, Robert, Kelley, Keith W., Craig, A. D. (Bud), 2012. Ten years of nature reviews neuroscience: insights from the highly cited. Nat. Rev. Neurosci. 11 (10), 718–726. https://doi.org/10.1038/nrn2912.Ten.

Mahjoory, Keyvan, Nikulin, Vadim V., Botrel, LoÃc, Linkenkaer-Hansen, Klaus, Fato, Marco M., Haufe, Stefan, 2017. Consistency of EEG source localization and connectivity estimates. Neuroimage 152, 590–601. ISSN 1053–8119. https://doi.org/10.1016/j.neuroimage.2017.02.076. http://www.sciencedirect.com/science/article/pii/S1053811917301854.

Marzetti, Laura, Del, Cosimo, Guido, Nolte, 2008. Understanding brain connectivity from EEG data by identifying systems composed of interacting sources. NeuroImage 42, 87–98. https://doi.org/10.1016/j.neuroimage.2008.04.250.

Matias Palva, J., Wang, Sheng H., Palva, Satu, Alexander, Zhigalov, Monto, Simo, Brookes, Matthew J., Schoffelen, Jan-Mathijs, Jerbi, Karim, 2018. Ghost interactions in Meg/EEG source space: a note of caution on inter-areal coupling measures. Neuroimage ISSN 1053–8119. https://doi.org/10.1016/j.neuroimage.2018.02.032. http://www.sciencedirect.com/science/article/pii/S1053811918301290.

Moran, R.J., Campo, P., Maestu, F., Reilly, R.B., Dolan, R.J., Strange, B.A., 2010. Peak frequency in the theta and alpha bands correlates with human working memory capacity. Front. Hum. Neurosci. 200 (4) https://doi.org/10.3389/fnhum.2010.00200.

Mosher, John C., Leahy, Richard M., Lewis, Paul S., 1999. EEG and MEG: forward solutions for inverse methods. IEEE Trans. Biomed. Eng. 46 (3), 245–259.

Mosher, J.C., Leahy, R.M., Feb 1999. Source localization using recursively applied and projected (rap) music. *Signal Processing*. IEEE Transactions on 47 (2), 332–340. https://doi.org/10.1109/78.740118. ISSN 1053–587X.

Nolte, G., Bai, O., Wheaton, L., Mari, Z., Vorbach, S., Hallett, M., 2004a. Basic mathematical and electromagnetic concepts of the biomagnetic inverse problem. Phys. Med. Biol. 115 (10), 2292–2307. http://www.ncbi.nlm.nih.gov/pubmed/15351371.

Nolte, G., Bai, O., Wheaton, L., Mari, Z., Vorbach, S., Hallett, M., 2004b. Identifying true brain interaction from EEG data using the imaginary part of coherency. Clin. Neurophysiol. 115 (10), 2292–2307. http://www.ncbi.nlm.nih.gov/pubmed/15351371.

O'Neill, George C., Barratt, Eleanor L., Tewarie, Prejaas K., E Hunt, Benjamin A., Brookes, Matthew J., 2015. Measuring electrophysiological connectivity by power envelope correlation: a technical review on MEG methods. Phys. Med. Biol. https://doi.org/10.1088/0031-9155/60/21/R271.

Ossadtchi, A., Greenblatt, R.E., Towle, V.L., Kohrman, M.H., Kamada, K., 2010. Inferring spatiotemporal network patterns from intracranial EEG data. Clin. Neurophisol. 121 (6), 823–835. http://www.sciencedirect.com/science/article/pii/S1388245710000350.

Pikovsky, A., Rosenblum, M., Kurths, J., 2001. Synchronization. A Universal Concept in Nonlinear Sciences. Cambridge University Press, Cambridge.

Rajagovindan, R., Ding, M., 2008. Decomposing neural synchrony: toward an explanation for near-zero phase-lag in cortical oscillatory networks. PLoS One 3 (11), e3649. http://www.ncbi.nlm.nih.gov/pubmed/18987745.

Roelfsema, P., Engel, A., Knig, P., Singer, W., 1997. Visuomotor integration is associated with zero time-lag synchronization among cortical areas. Nature 385 (6612), 157–161. http://www.ncbi.nlm.nih.gov/pubmed/8990118.

Schnitzler, Alfons, Gross, Joachim, 2005. Normal and Pathological Oscillatory Communication in the Brain. Nat. Rev. Neurosci. 6 (April) https://doi.org/10.1038/nrn1650.

Schoffelen, Jan-mathijs, Gross, Joachim, 2009. Source Connectivity Analysis with MEG and EEG. Hum. Brain Mapp. 1857–1865. https://doi.org/10.1002/hbm.20745.

Schuster, H.G., Wagner, P., 1989. Mutual entrainment of two limit cycle oscillators with time delayed coupling. Prog. Theor. Phys. 81 (5).

Singer, W., 1999. Neuronal synchrony: a versatile code for the definition of relations? Neuron 1999 (24), 49–65, 1999.

Soto, Juan L.P., Lachaux, Jean-philippe, Sylvain Baillet, Jerbi, Karim, 2016. A multivariate method for estimating cross-frequency neuronal interactions and correcting linear mixing in MEG data , using canonical correlations. J. Neurosci. Meth. 271, 169–181. https://doi.org/10.1016/j.jneumeth.2016.07.017. ISSN 0165–0270. https://doi.org/10.1016/j.jneumeth.2016.07.017.

Stam, C.J., Nolte, G., Daffertshofer, A., 2007. Phase lag index: assessment of functional connectivity from multi channel EEG and MEG with diminished bias from common sources. Hum. Brain Mapp. 28 (11), 1178–1193. http://www.ncbi.nlm.nih.gov/pubmed/17266107.

Striem-Amit, Ella, Vannuscorps, Gilles, Caramazza, Alfonso, 2017. Sensorimotor-independent development of hands and tools selectivity in the visual cortex. Proc. Natl. Acad. Sci. Unit. States Am. 114 (18), 4787–4792. http://www.pnas.org/content/114/18/4787.abstract.

Strohmeier, D., Bekhti, Y., Haueisen, J., Gramfort, A., Oct 2016. The iterative reweighted mixed-norm estimate for spatio-temporal meg/eeg source reconstruction. IEEE Trans. Med. Imag. 35 (10), 2218–2228. https://doi.org/10.1109/TMI.2016.2553445. ISSN 0278–0062.

van den Heuvel, Martin P., Kahn, Rene S., Goni, Joaqin, Sporns, Olaf, 2012. High-cost, high-capacity backbone for global brain communication. *PNAS*. Proc. Natl. Acad. Sci. Unit. States Am. 109 (28), 11372–11377. http://www.pnas.org/content/109/28/11372.abstract.

Varela, F., Lachaux, J.P., Rodriguez, E., Martinerie, J., 2001. The brainweb: phase synchronization and large-scale integration. Nat. Rev. Neurosci. 2 (April), 229–239. http://www.nature.com/nrn/journal/v2/n4/full/nrn0401_229a.html.

Vinck, M., Oostenveld, R., van Wingerden, M., Battaglia, F., Pennartz, C.M., 2011. Ban improved index of phase-synchronization for electrophysiological data in the presence of volume-conduction, noise and sample-size bias. Neuroimage 55 (4), 1548–1565. http://www.ncbi.nlm.nih.gov/pubmed/21276857.

Wang, Sheng H., Lobier, Muriel, Siebenhühner, Felix, Puoliväli, Tuomas, Palva, Satu, Matias Palva, J., 2018. Hyperedge bundling: a practical solution to spurious interactions in Meg/EEG source connectivity analyses. Neuroimage. ISSN 1053–8119. https://doi.org/10.1016/j.neuroimage.2018.01.056. http://www.sciencedirect.com/science/article/pii/S1053811918300569.

Wens, V., Brice, M., Mary, A., Bourguignon, M., Beeck, M., Goldman, S., Bogaert, P., Peigneux, P., De Tie, X., 2015. A geometric correction scheme for spatial leakage effects in MEG/EEG seed-based functional connectivity mapping. Hum. Brain Mapp. 4621 (August), 4604–4621. https://doi.org/10.1002/hbm.22943.

Wibral, M., Rahm, B., Rieder, M., Lindner, M., Vicente, R., Kaiser, J., 2011. Transfer entropy in magnetoencephalographic data: quantifying information flow in cortical and cerebellar networks. Prog. Biophys. Mol. Biol. 105 (1–2), 80–97. http://www.scopus.com/inward/record.url?eid=2-s2.0-79555168971&partnerID=40&md5=31bfe00660c19cb98378965b389b5a0c. cited By (since 1996)26.

Zalesky, Andrew, Cocchi, Luca, Fornito, Alex, Micah, M. Murray, Bullmore, Ed, 2012. Connectivity differences in brain networks. Neuroimage 60 (2), 1055–1062. https://doi.org/10.1016/j.neuroimage.2012.01.068. ISSN 10538119. https://doi.org/10.1016/j.neuroimage.2012.01.068.